JGR Solid Earth

RESEARCH ARTICLE
10.1029/2021JB023133

Phase Transitions of Fe-, Al- and Ca-Bearing Orthopyroxenes at High Pressure and High Temperature: Implications for Metastable Orthopyroxenes in Stagnant Slabs

Jingui Xu[1,2], Dawei Fan[1], Dongzhou Zhang[2], Maining Ma[3], Yi Zhou[4], Sergey N. Tkachev[5], Wenge Zhou[1], and Przemyslaw K. Dera[2]

[1]Key Laboratory for High-Temperature and High-Pressure Study of the Earth's Interior, Institute of Geochemistry, Chinese Academy of Sciences, Guiyang, China, [2]Hawai'i Institute of Geophysics and Planetology, School of Ocean and Earth Science and Technology, University of Hawai'i at Manoa, Honolulu, HI, USA, [3]Key Laboratory of Computational Geodynamics, College of Earth and Planetary Sciences, University of Chinese Academy of Sciences, Beijing, China, [4]School of Geoscience and Technology, Southwest Petroleum University, Chengdu, China, [5]Center for Advanced Radiation Sources, University of Chicago, Chicago, IL, USA

Key Points:

- Single-crystal X-ray diffraction experiments were carried out on Fe-, Al- and Ca-bearing orthopyroxenes under high *P-T* conditions
- Compositional and temperature effects on the phase transitions and equations of state of orthopyroxenes were investigated
- β-opx and γ-opx are possible metastable phases of natural orthopyroxenes within cold stagnant slabs

Supporting Information:

Supporting Information may be found in the online version of this article.

Correspondence to:

J. Xu and D. Fan,
xujingui@hawaii.edu;
fandawei@vip.gyig.ac.cn

Citation:

Xu, J., Fan, D., Zhang, D., Ma, M., Zhou, Y., Tkachev, S. N., et al. (2022). Phase transitions of Fe-, Al- and Ca-bearing orthopyroxenes at high pressure and high temperature: Implications for metastable orthopyroxenes in stagnant slabs. *Journal of Geophysical Research: Solid Earth*, *127*, e2021JB023133. https://doi.org/10.1029/2021JB023133

Received 30 AUG 2021
Accepted 10 JAN 2022

Abstract The phase transitions of natural San Carlos Fe-, Al- and Ca-bearing orthopyroxene and two synthetic orthopyroxenes containing Al (up to 12 wt. % Al_2O_3) and Fe (up to 15 wt. % FeO) were investigated at high pressures and temperatures up to ~30 GPa and 700 K using synchrotron-based single-crystal X-ray diffraction. These orthopyroxenes undergo α-opx → β-opx → γ-opx phase transitions with increasing pressure and temperature. We quantitatively described how the composition influences the pressures of the phase transitions. The results indicated that the variations in Mg, Fe, and Al contents do not significantly influence the pressure of the α-opx → β-opx transition ($P_{\alpha\text{-}\beta}$). For the β-opx → γ-opx phase transition, increasing Fe content decreases the $P_{\beta\text{-}\gamma}$ while increasing Al content increases the $P_{\beta\text{-}\gamma}$. The incorporation of Ca increases the $P_{\alpha\text{-}\beta}$ and decreases the $P_{\beta\text{-}\gamma}$. The thermal equations of states of α-opx and β-opx for these three orthopyroxenes were determined using the unit-cell volume collected at high pressures and temperatures, which have been used to establish a density model to interpret the cold stagnant slabs. Our experimental results have indicated that β-opx and γ-opx are possible metastable phases of natural orthopyroxenes within cold stagnant slabs in the mantle transition zone.

Plain Language Summary Orthopyroxene ((Mg, Fe, Ca)(Mg, Fe, Al)(Si, Al)$_2O_6$) is a major rock-forming mineral in subducting slabs, and its metastable phases are considered to be related to the stagnation of slabs which are located at the transition zone due to its low density in comparison to other major slab minerals. Studies on the phase transitions of orthopyroxenes under the pressure-temperature conditions of subducting slabs are necessary to understand the metastable phases of orthopyroxenes within stagnant slabs. Here, for the first time, we investigated the phase transitions of natural and synthetic orthopyroxenes in a large range of compositional variations under the pressure-temperature conditions present in extremely cold subducting slabs up to the bottom of Earth's transition zone. The results indicated that the α-opx → β-opx → γ-opx phase transitions could occur for natural orthopyroxenes under such pressure-temperature conditions. Therefore, the β-opx and γ-opx are possible metastable phases of orthopyroxenes within stagnant slabs in the transition zone. Using the obtained thermal equation of state of orthopyroxene and its high-pressure phases together with literature results, we modeled the densities of cold subducting slab which includes metastable orthopyroxene and olivine. We show that the existence of metastable orthopyroxene and olivine could result in slab stagnation within the upper range of the transition zone.

1. Introduction

Orthopyroxene is an important mineral in the typical peridotite and pyroxenite of Earth's upper mantle, and it also occurs as a constituent of many other types of igneous and metamorphic rocks, for example, gabbro, diorite, basalt, andesite, dacite, and granulite (Nesse, 2000). Orthopyroxene is found as typical inclusion in lithospheric diamonds (Nestola, 2015; Stachel & Harris, 2008) and super-deep diamonds (Smith et al., 2018; Walter et al., 2011), indicating that it is a common mineral in the mantle. In addition, orthopyroxene is an abundant mineral in many meteorites and interplanetary dust particles (e.g., Hazen et al., 2008).

Owing to its abundance in the Earth's upper mantle (the volume content can be as high as 40% in mantle peridotite; Bodinier & Godard, 2007; Faccincani et al., 2021), orthopyroxene has been extensively investigated at high pressure (*P*) and high temperature (*T*) to understand its phase transitions and elastic properties. Under normal mantle geotherms, orthopyroxene transforms from the orthorhombic phase with *Pbca* symmetry into monoclinic clinopyroxene with *C*2/*c* symmetry at depths of approximately 250 km (e.g., Akashi et al., 2009; Shinmei et al., 1999); with increasing depth, it gradually dissolves into majoritic garnets and is exhausted in the transition zone (Ita & Stixrude, 1992). Geophysical observations and modeling show that the upper mantle and transition zone are heterogeneous in both temperature and chemical content. For instance, widespread stagnant slabs are found in the transition zone regions of many cold subduction zones (e.g., Fukao & Obayashi, 2013). Based on geophysical and geodynamic modeling, the temperatures in these stagnant slabs are much lower than those in the normal mantle. For example, slab stagnation in the transition zone exists in the Tonga subduction system (Fukao & Obayashi, 2013; Liu et al., 2021) and the temperature of the Tonga slab is estimated to be ~800 K at 600 km (Ganguly et al., 2009; King et al., 2015). Experimental studies on the diffusion of majorite suggest that pyroxene minerals could be preserved within slabs as metastable phases at transition zone depths in cold subduction zones (Nishi et al., 2013; Van Mierlo et al., 2013). These observations have inspired many experimental and computational studies on the metastable phases of pyroxene minerals at high *P* and relatively low *T* and the effects of their metastability on slab dynamics (e.g., Agrusta et al., 2014; Faccenda & Dal Zilio, 2017; King et al., 2015; Xu et al., 2019).

(Mg, Fe)SiO_3 is generally referred to as the chemical composition of mantle orthopyroxene (e.g., Frost, 2008), whereas other cationic elements (e.g., Al and Ca) also prevail. The phase transitions of Mg and Fe-endmembers, as well as their solid solutions, have been extensively investigated at both room *T* (e.g., Hugh-Jones et al., 1996; Kung & Li, 2014; Li et al., 2014; Serghiou et al., 2000; Zhang et al., 2011; Zhang et al., 2012; Zhang et al., 2014; Zhang & Bass, 2016; Zhang, Reynard, et al., 2013) and high *T* (e.g., Kung et al., 2004; Wang et al., 2019; Xu et al., 2018; Xu et al., 2020; Zhang et al., 2014) by various techniques, for example, X-ray diffraction (XRD), ultrasonic interferometry (UI), Raman spectroscopy, Brillouin spectroscopy (BS), and nuclear resonant inelastic X-ray scattering spectroscopy. High *P*-*T* single-crystal (SC) XRD experiments have revealed the phase transition path of (Mg, Fe)SiO_3 orthopyroxene, which transforms from the initial α-opx (*Pbca*) to β-opx ($P2_1/c$; Zhang et al., 2012) and then, depending on the iron content, transforms either to $P2_1ca$ (α-popx; Finkelstein et al., 2015) or to *Pbca* symmetry (γ-opx; Dera, Finkelstein, et al., 2013). The iron content also decreases the onset pressure of these phase transitions (Xu et al., 2020; Zhang, Reynard, et al., 2013).

Numerous studies have reported Al-bearing orthopyroxenes in various geological settings. Orthopyroxene in mantle peridotites generally contains Al_2O_3 up to ~7 wt. % (e.g., Arai & Abe, 1995). Al-bearing orthopyroxene is also not uncommon in mantle pyroxenite xenoliths, and the highest content of Al_2O_3 reaches ~12 wt. % (e.g., Stachel & Harris, 2008). Al-bearing orthopyroxene (higher than 10 wt. % Al_2O_3) has also been reported in high-*P* metamorphic rocks (e.g., Belyanin et al., 2012) and some interplanetary dust particles (Klöck et al., 1989). Thus, it is necessary to investigate the high-*P* behavior of orthopyroxenes with various contents of Al_2O_3 to evaluate the effects of Al on the phase stability. The Ca content in orthopyroxene is usually much lower than that of Fe and Al. The CaO content is generally lower than 1 wt. % (Stachel & Harris, 2008).

To date, several studies have investigated the phase transition of Al-bearing orthopyroxenes. Zhang, Reynard, et al. (2013) investigated the phase transition of natural orthopyroxene with moderate content of Al_2O_3 (~5 wt. %) and CaO (~1 wt. %) under room *T* and high *P* up to 18 GPa using Raman spectroscopy, and they suggested that Al and Ca increase the pressure of the phase transition. Subsequently, with the same method, the phase transition of a natural Fe-, Al-, and Ca-bearing orthopyroxene (San Carlos, Arizona) was investigated under high *P* and high *T* up to 18 GPa and 673 K (Zhang et al., 2014). In addition, several other studies (Chai et al., 1997; Hua et al., 2020; Hugh-Jones et al., 1997; Hugh-Jones & Angel, 1997; Xu et al., 2016; Xu, Ma, et al., 2017) investigated natural or synthetic Al-bearing orthopyroxene with various Al_2O_3 contents (<5 wt. %) at high *P*, and no phase transition was observed within their experimental pressure range (<13 GPa). Therefore, existing studies cannot provide precise information on the metastable phases of orthopyroxenes with large chemical (Fe, Al, and Ca) variation within the stagnant slabs where the pressure could be well above 20 GPa.

To investigate possible metastable phases of orthopyroxenes with complex chemical compositions comparable to those of natural orthopyroxenes within extremely cold stagnant slabs, in this study, synchrotron-based SCXRD experiments were carried out on a natural Fe-, Al, and Ca-bearing San Carlos orthopyroxene and two synthetic

Fe- and Al-bearing orthopyroxenes with different Al_2O_3 contents (5–12 wt. %) at various *P-T* conditions (up to ~30 GPa and 700 K). The obtained results were used to model the density profile of cold subducting slab which incorporates the metastable orthopyroxene. In addition, the role of metastable orthopyroxene and its high-*P* phases in the slab stagnation within the transition zone was discussed.

2. Sample and Experimental Methods

Three orthopyroxenes with different Al_2O_3 contents were investigated in this study. The first was a natural San Carlos orthopyroxene (Al-opx#1, $Na_{0.005}Ca_{0.02}Mg_{0.82}Fe_{0.09}Cr_{0.005}Al_{0.11}Si_{0.95}O_3$); the chemical composition expressed in end-member molar percentages (M; mol. %) is $En_{79}Fs_9MgTs_{10}Wo_2$, where En = enstatite ($MgSiO_3$), Fs = ferrosilite ($FeSiO_3$), MgTs = Mg-tschermakite ($Mg_{0.5}Al_{0.5}Si_{0.5}Al_{0.5}O_3$), and Wo = wollastonite ($CaSiO_3$). The other two were synthetic orthopyroxenes, Al-opx#2 ($Mg_{0.72}Fe_{0.23}Al_{0.10}Si_{0.95}O_3$ or $En_{67}Fs_{23}MgTs_{10}$) and Al-opx#3 ($Mg_{0.80}Fe_{0.08}Al_{0.24}Si_{0.88}O_3$ or $En_{68}Fs_8MgTs_{24}$). The synthetic methods are similar to those of our previous study (Xu et al., 2018). The chemical compositions are derived from the results of electron microprobe analyses (EMPA; Table S1 in the Supporting Information S1). The analyses were carried out with a JXA 8230 operating at an acceleration voltage of 15 kV with a beam current of 20 nA, and the focused electron beam was ~5 μm.

Crystals with high-quality diffraction peaks were selected for the ambient and high *P-T* SCXRD experiments (Figure S1 in the Supporting Information S1). Polymer micromesh sample holders (MiTeGen) were used to mount the crystals of $En_{67}Fs_{23}MgTs_{10}$ and $En_{68}Fs_8MgTs_{24}$, while the ambient measurement of $En_{79}Fs_9MgTs_{10}Wo_2$ was performed in a diamond anvil cell (DAC). Two types of DACs were used: short symmetric DACs equipped with Boehler-Almax-type diamonds and WC seats were used for the room-*T* high-*P* SCXRD experiments, while externally heated DACs (EHDAC) was used for high *P-T* experiments. For each DAC, a gold foil and a crystal were loaded together into the sample chamber followed by gas loading with neon as the pressure medium using the GSECARS gas loading system (Rivers et al., 2008). A detailed description of the sample preparation can be found in our previous studies (e.g., Xu, Zhang, et al., 2017).

Several runs of experiments were conducted for the orthopyroxenes to investigate their phase transitions and thermal equation of state (EoS) at high *P-T* conditions. In the first run (run #1), room-*T* high-*P* SCXRD experiments were performed on $En_{67}Fs_{23}MgTs_{10}$ and $En_{68}Fs_8MgTs_{24}$ up to 32.6 and 35.1 GPa, respectively. The high *P-T* experiments of $En_{67}Fs_{23}MgTs_{10}$ and $En_{68}Fs_8MgTs_{24}$ up to 13.4 GPa and 700 K were performed in run #2. In run #3, the SCXRD data were collected at high *P-T* up to 29.5 GPa and 700 K for $En_{68}Fs_8MgTs_{24}$. The SCXRD experiments of $En_{67}Fs_{23}MgTs_{10}$ at high *P-T* up to 24.4 GPa and 700 K were performed in run #4. In run #5, room-*T* high-*P* SCXRD experiments were performed on $En_{79}Fs_9MgTs_{10}Wo_2$ up to 34.8 GPa. The high *P-T* experiments for the $En_{79}Fs_9MgTs_{10}Wo_2$ up to 25.0 GPa and 700 K were performed in run #6.

All the experiments except for run #3 were performed at the 13-BM-C experimental station of the Advanced Photon Source, Argonne National Laboratory. The incident X-ray beam at 13-BM-C was monochromated to 0.4340 Å with a focal spot size of 12 × 18 μm^2. Different detectors (MAR 165 CCD for run #1 and run #4 and Pilatus 1 M for run #2, run #5 and run #6) were used for these experiments. A detailed description of the experimental procedures at 13-BM-C can be found in the report by Zhang et al. (2017). The high *P-T* experiments on $En_{68}Fs_8MgTs_{24}$ (run #3) were performed at the 13-BM-D experimental station of the Advanced Photon Source, Argonne National Laboratory. The incident X-ray had a wavelength of 0.3344 Å and a beam size of 3 × 7 μm^2. The diffraction images were acquired using a stationary Perkin-Elmer area detector. The diffraction images collected by the Pilatus 1 M detector were analyzed by the APEX3 Crystallography Software Suite, while the GSE_ADA/RSV (Dera, Zhuravlev, et al., 2013) software package was employed to process the data collected by the MAR165 CCD and Perkin-Elmer area detectors.

3. Results

3.1. Ambient SCXRD

The ambient SCXRD data were used to refine the structures of $En_{67}Fs_{23}MgTs_{10}$ and $En_{68}Fs_8MgTs_{24}$. We did not refine the structure of $En_{79}Fs_9MgTs_{10}Wo_2$ under ambient conditions because it was investigated in a previous study (Zhang et al., 2012). The crystal structures of $En_{67}Fs_{23}MgTs_{10}$ and $En_{68}Fs_8MgTs_{24}$ were refined using Shelxl software (Sheldrick, 2008) facilitated by the Olex 2 user interface (Dolomanov et al., 2009). Orthopyroxene has

a general formula of M2M1T1T2O_6 according to previous studies (e.g., Periotto et al., 2012). The EMPA results were used to constrain the atomic fractions of the cations when we refined the site occupancies. Cations sitting at the same site were constrained to share the same atomic coordinates and displacement parameters. The structural refinements show that Al prefers to enter the M1 site rather than the M2 site in both orthopyroxenes, as the Al occupancy in the M2 site is below the detection limit of the diffraction, which is very consistent with those of previous studies on Al-bearing orthopyroxenes (e.g., Nestola et al., 2008; Tarantino et al., 2002). Moreover, Al prefers the T2 site in $En_{67}Fs_{23}MgTs_{10}$, which is consistent with the results of previous studies on orthopyroxenes with similar Al contents (Al_2O_3 < 5 wt. % (Nestola et al., 2008; Tarantino et al., 2002). Therefore, the occupancies of Al in the M1 and T2 sites were fixed according to the EMPA results when we refined the structure of $En_{67}Fs_{23}MgTs_{10}$ (Table S2a in the Supporting Information S1). Following the same procedure as for $En_{67}Fs_{23}MgTs_{10}$, the structure of $En_{68}Fs_8MgTs_{24}$ was refined. The M1 site occupancy of Al in $En_{68}Fs_8MgTs_{24}$ was similar to that in $En_{67}Fs_{23}MgTs_{10}$, and no Al resides on the M2 site. However, in $En_{68}Fs_8MgTs_{24}$, a significant amount of Al resides on the T1 site in addition to the T2 site, indicating that the occupancies in the *T* sites of Mg-Fe-Al orthopyroxene depend upon the Al content. In the refinement of the $En_{68}Fs_8MgTs_{24}$ structure, the occupancy of Al in the M1 site was fixed according to the EMPA results (Table S2b in the Supporting Information S1).

3.2. Phase Transition at Room-*T* High-*P*

The room-*T* high-*P* data indicated that $En_{79}Fs_9MgTs_{10}Wo_2$ underwent two phase transitions with increasing pressure up to 34.8 GPa. As shown in Figure S2a in the Supporting Information S1, the diffraction image did not change significantly with increasing pressure up to 15.5 GPa, and the diffraction peaks were perfectly indexed with the initial orthorhombic *Pbca* unit cell (α-opx). Up to that pressure, the unit-cell parameters decreased smoothly with increasing pressure (Figure S3a in the Supporting Information S1). After 15.5 GPa, new peaks emerged, and the peaks of α-opx disappeared, indicating a phase transition. The new peaks were successfully indexed with a monoclinic unit cell that is similar to that of the β-opx phase reported in previous studies (Dera, Finkelstein, et al., 2013; Zhang et al., 2012). The peak indexing indicated that pseudo-merohedral twinning existed in the high-*P* phase, as indicated by the two symmetrically related crystal domains shown in the diffraction image (Figure S2a in the Supporting Information S1). The structural refinement failed to converge for this high-*P* phase due to the substantial peak overlap caused by the twinning, but the analysis of the space group suggested that it had the same symmetry ($P2_1/c$) as the β-opx phase. Moreover, the diffraction images and unit-cell parameters of this high-*P* phase of $En_{79}Fs_9MgTs_{10}Wo_2$ were similar to those of the β-opx phase (Dera, Finkelstein, et al., 2013; Xu et al., 2018; Zhang et al., 2012); therefore, this high-*P* phase is isostructural with the β-opx phase.

The β-opx phase of $En_{79}Fs_9MgTs_{10}Wo_2$ persisted up to 26.3 GPa with unit-cell parameters *a*, *b* and *c* decreasing with pressure, while its β angle increased slightly (Figure S3a in the Supporting Information S1). At 29.7 GPa, the number of peaks largely decreased (Figure S2a in the Supporting Information S1). Indexing the peaks resulted in an orthorhombic unit cell, and the twinning observed in the β-opx phase disappeared (Figure S2a in the Supporting Information S1). No further phase transitions were observed up to 34.8 GPa. The structure of this high-*P* phase was solved and refined with *Pbca* symmetry (Table S3a in the Supporting Information S1) using diffraction data collected at 28.1 GPa during the decompression. This structure is the same as that of the γ-opx phase previously observed in Fe-rich orthopyroxene at high *P* (Dera, Finkelstein, et al., 2013; Xu et al., 2020).

The phase transition path of $En_{67}Fs_{23}MgTs_{10}$ was similar to that of $En_{79}Fs_9MgTs_{10}Wo_2$ (Figure 3b). The β-opx phase occurred at 14.9 GPa, and the γ-opx phase (Table S3b in the Supporting Information S1) emerged at 32.6 GPa. However, $En_{68}Fs_8MgTs_{24}$ underwent only one phase transition as the pressure increased from room *P* to 35.1 GPa. At 15.7 GPa, β-opx emerged and survived up to the maximum pressure (Figure S2c in the Supporting Information S1). Its β angle increased, and its unit-cell parameters *a*, *b* and *c* decreased with increasing pressure (Figure S3c in the Supporting Information S1).

The unit-cell parameters and volume varied discontinuously through the phase transitions (Figure S3 in the Supporting Information S1), indicating that these phase transitions are first order. As shown in Figure 1 and Figure S3 in the Supporting Information S1, in the α-opx → β-opx transition, the unit-cell volume of $En_{79}Fs_9MgTs_{10}Wo_2$, $En_{67}Fs_{23}MgTs_{10}$ and $En_{68}Fs_8MgTs_{24}$ dropped by 1.1%, 1.1% and 1.2%, respectively. In the β-opx → γ-opx transition, the unit-cell volume drops of $En_{79}Fs_9MgTs_{10}Wo_2$ and $En_{67}Fs_{23}MgTs_{10}$ were 1.8% and 2.4%, respectively. The unit-cell parameters *a*, *b* and *c* behaved very similarly for $En_{79}Fs_9MgTs_{10}Wo_2$, $En_{67}Fs_{23}MgTs_{10}$ and $En_{68}Fs_8MgTs_{24}$ in the α-opx → β-opx transition. Unit-cell parameter *a* increased by 0.5%, 0.9% and 0.9%, and *c* decreased by

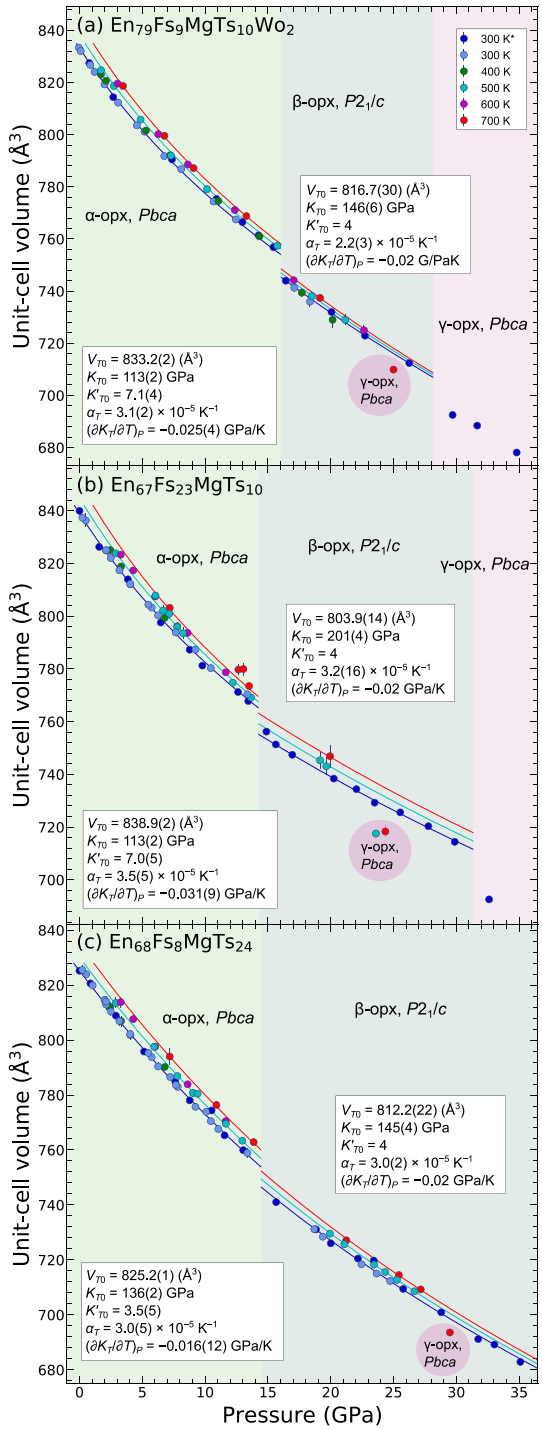

Figure 1. The unit-cell volumes of $En_{79}Fs_9MgTs_{10}Wo_2$ (a), $En_{67}Fs_{23}MgTs_{10}$ (b) and $En_{68}Fs_8MgTs_{24}$ (c) as a function of pressure and temperature. The light blue, green, cyan, magenta, and red symbols represent the measured unit-cell volumes at 300 K, 400 K, 500 K, 600 K, and 700 K, respectively, in the high *P-T* experiments; the deep blue symbols represent data collected in the room-*T* high-*P* experiments. The shaded areas indicate the regions of the α-opx, β-opx, and γ-opx phases. The space group of each phase is also shown. The thermal EoS parameters, including V_{T0}, K_{T0}, K'_{T0}, α_T, and $(\partial K_T/\partial T)_P$, are shown for α-opx and β-opx. The blue, cyan, and red lines represent the isothermal compression curves at 300 K, 500 K, and 700 K, respectively; these were calculated by using the thermal EoS parameters. Error bars smaller than the symbol size are not shown.

1.8%, 2.3% and 2.2% for $En_{79}Fs_9MgTs_{10}Wo_2$, $En_{67}Fs_{23}MgTs_{10}$ and $En_{68}Fs_8MgTs_{24}$, respectively, while b varied much more continuously. In the β-opx → γ-opx transition of $En_{79}Fs_9MgTs_{10}Wo_2$ and $En_{67}Fs_{23}MgTs_{10}$, the unit-cell volume dropped by 1.8% and 2.4%, c dropped by 2.0% and 2.3%, respectively, and a and b varied much more continuously (Figure S3 in the Supporting Information S1).

3.3. Phase Transition at High *P-T*

The diffraction data collected at high *P-T* conditions for $En_{79}Fs_9MgTs_{10}Wo_2$, $En_{67}Fs_{23}MgTs_{10}$, and $En_{68}Fs_8MgTs_{24}$ indicated that each sample underwent two phase transitions (Figure S4 in the Supporting Information S1). No structural refinement was performed for the samples at high *P-T* because the number of diffraction peaks collected at high *P-T* was very limited due to the limited opening angle of the used EHDAC. Nonetheless, the peak indexing and space group analyses indicated that the high-*P* phases observed at high *P-T* were the same as those observed at room-*T* high-*P*. The diffraction peaks of the high-*P* phases were successfully indexed with β-opx and γ-opx (Figures 1 and S4 in the Supporting Information S1). The α-opx → β-opx and β-opx → γ-opx phase transitions were observed for all three orthopyroxenes (Figure S4 in the Supporting Information S1). The β-opx phase occurred at 17.1 GPa/600 K, 20.0 GPa/700 K, and 19.9 GPa/500 K for $En_{79}Fs_9MgTs_{10}Wo_2$, $En_{67}Fs_{23}MgTs_{10}$, and $En_{68}Fs_8MgTs_{24}$, respectively (Figure S5 in the Supporting Information S1). Similar to the room-*T* high-*P* experiments, the β-opx phase occurred as pseudo-merohedral twinning for all three samples at high *P-T* (Figure S4 in the Supporting Information S1). The γ-opx phase occurred at 25.0 GPa/700 K, 24.4 GPa/700 K and 29.5 GPa/700 K for $En_{79}Fs_9MgTs_{10}Wo_2$, $En_{67}Fs_{23}MgTs_{10}$, and $En_{68}Fs_8MgTs_{24}$, respectively (Figures S4 and S5 in the Supporting Information S1).

3.4. Thermal Equation of State

The thermal EoS parameters of the α-opx and β-opx phases of $En_{79}Fs_9MgTs_{10}Wo_2$, $En_{67}Fs_{23}MgTs_{10,}$ and $En_{68}Fs_8MgTs_{24}$ were determined by fitting the high *P-T* unit-cell volume (*P-V-T*) data (Table S4 in the Supporting Information S1) to the high-*T* third-order Birch-Murnaghan EoS (BM3 EoS). The high-*T* BM3 EoS (Birch, 1947) is defined as follows (1–3):

$$P = \frac{3K_{T0}}{2}\left[\left(\frac{V_{T0}}{V}\right)^{\frac{7}{3}} - \left(\frac{V_{T0}}{V}\right)^{\frac{5}{3}}\right]\left\{1 + \frac{3}{4}\left(K'_{T0} - 4\right)\left[\left(\frac{V_{T0}}{V}\right)^{\frac{2}{3}} - 1\right]\right\} \quad (1)$$

where V_{T0} is the unit-cell volume at zero pressure at T, K_{T0} is the isothermal bulk modulus, K'_{T0} is the pressure derivative of K_{T0}, and P and V are the measured pressure and unit-cell volume in the experiments, respectively (Table S4 in the Supporting Information S1). The K_{T0} in Equation 1 is assumed to be a linear function of temperature:

$$K_{T0} = K_{300,0} + (\partial K_T/\partial T)_P(T - 300) \quad (2)$$

where $K_{300,\,0}$ is the isothermal bulk modulus at room *P-T*, and $(\partial K_T/\partial T)_P$ is the temperature derivative of the isothermal bulk modulus. V_{T0} in Equation 1 is expressed as a function of the thermal expansion coefficient (α_T):

$$V_{T0} = V_{300,0}exp\int_{300}^{T}\alpha_T dT \quad (3)$$

where $V_{300,0}$ is the unit-cell volume at room *P-T*. In this study, the effects of temperature on α_T are not considered due to the limited number of high-*T* data points.

The obtained thermal EoS parameters of the α-opx phase for $En_{79}Fs_9MgTs_{10}Wo_2$, $En_{67}Fs_{23}MgTs_{10}$ and $En_{68}Fs_8MgTs_{24}$ are summarized in Figure 1, showing that the K_{T0}, K'_{T0}, $(\partial K_T/\partial T)_{P,}$ and α_T are within 113(2) - 136(2) GPa, 3.5(5) - 7.1(4), −0.031(9) - −0.016(12) GPa/K and 3.0(2) - 3.5(5) × 10^{-5} K^{-1}, respectively. K'_{T0} was fixed at 4, and $(\partial K_T/\partial T)_P$ was fixed at −0.02 GPa/K (identical to the $(\partial K_T/\partial T)_P$ of the β-opx phase of En; Xu et al. (2018)) when we fitted the β-opx *P-T-V* data to the high-*T* BM3 EoS due to the limited data range (Figure 1). V_{T0}, K_{T0} and α_T were 803.9(14) - 816.7(30) $Å^3$, 145(4) - 201(4) GPa, and 2.2(3) - 3.2(16) × 10^{-5} K^{-1}, respectively.

4. Discussion

4.1. Compositional Effects on the Phase Transition of Orthopyroxene

The phase transitions of orthopyroxene with various compositions (Ca-Mg-Fe-Al) at room-*T* high-*P* are summarized in Figure 2. The first phase transition (α-opx → β-opx) is independent of the compositional variation, but the second phase transition is composition-dependent. As shown in Figure 2a, the α-opx → β-opx phase transition occurs for orthopyroxene with any compositions. Following the α-opx → β-opx phase transition, the β-opx → γ-opx phase transition occurs for orthopyroxenes whose M_{En} is lower than ~80, however, different phase transitions were observed for $En_{90}Fs_{10}$ and En (Figure 2a). Finkelstein et al. (2015) investigated the phase transitions of Al-free orthopyroxene ($En_{90}Fs_{10}$) up to 48.5 GPa at room-*T* using SCXRD. They did not observe the β-opx → γ-opx phase transition; instead, $En_{90}Fs_{10}$ underwent the β-opx → α-popx phase transition at 26.9–29.9 GPa followed by a third phase transition (α-popx → β-popx) at 36.8–40.3 GPa. In addition, Serghiou et al. (2000) performed a high-*P* Raman spectroscopic study on En to 70 GPa and identified two phase transitions at 7–15 GPa and 38–40 GPa. The first phase transition was the α-opx → β-opx phase transition, as confirmed by SCXRD experiments (Xu et al., 2018), and the second phase transition was likely the β-opx → β-popx phase transition, as octahedrally-coordinated Si, which is similar to the Si in the β-popx phase of the $En_{90}Fs_{10}$ (Finkelstein et al., 2015), emerged after the phase transition (Serghiou et al., 2000).

The compositional effects on the pressures of the phase transitions of orthopyroxene have been qualitatively described in previous studies. Generally, increasing the Fe content decreases the pressures ($P_{\alpha\text{-}\beta}$ and $P_{\beta\text{-}\gamma}$) of the α-opx → β-opx and β-opx → γ-opx phase transitions, while the effects of Al are the opposite (Xu et al., 2020; Zhang, Reynard, et al., 2013). The addition of new data (Figure 2 and Table S5 in the Supporting Information S1) in this study allows a more quantitative description of the compositional effects on the $P_{\alpha\text{-}\beta}$ and $P_{\beta\text{-}\gamma}$.

We first investigated the compositional effects of Ca- and Al-free En-Fs solid solutions. The $P_{\alpha\text{-}\beta}$ and $P_{\beta\text{-}\gamma}$ are shown in Figure 2a as a function of M_{En}. As shown in Figure 2a, the $P_{\alpha\text{-}\beta}$ - M_{En} data follow different trends over different regions (M_{En} = 44–100 and M_{En} = 0–44) of the data. A linear fit of the $P_{\alpha\text{-}\beta}$ - M_{En} data (M_{En} = 44–100) yields the following equation: $P_{\alpha\text{-}\beta}$ (GPa) = 13.4(5) − 0.011(6)M_{En}, and R^2 = 0.43, and the end-member enstatite is excluded from the fit as the scattered results from different measurements lead to unreasonable fitting. Within the data range of M_{En} = 0–44, there are only two data points available, so we did not carry out a linear fitting; however, it is clear that the compositional effect within M_{En} = 0–44 is more significant than that within M_{En} = 44–100 (Figure 2a). In comparison to $P_{\alpha\text{-}\beta}$, $P_{\beta\text{-}\gamma}$ increases steadily with increasing M_{En} over the whole data range, as shown by the linear regression equation $P_{\beta\text{-}\gamma}$ (GPa) = 12.2(8) + 0.17(1)M_{En}, and R^2 = 0.98. Increasing M_{En} also increases the pressure of the third phase transition (α-popx → β-popx or β-opx → β-popx), though only two data points are available to date.

The $P_{\alpha\text{-}\beta}$ and $P_{\beta\text{-}\gamma}$ as a function of the M_{MgTs} are shown in Figure 2b. To determine the effects of variation of M_{MgTs} on $P_{\alpha\text{-}\beta}$ and to minimize the disturbance of the effects from other compositional changes (Fe and Ca), only the Ca-free data within M_{En} = 44–100 are considered, since varying M_{En} does not significantly shift $P_{\alpha\text{-}\beta}$ over this data range (Figure 2a). The Al-free data are averaged for the fitting. A linear fit to the data yields the equation $P_{\alpha\text{-}\beta}$ (GPa) = 12.9(8) + 0.08(6)M_{MgTs}, and R^2 = 0.64, indicating that increasing M_{MgTs} only weakly increase the $P_{\alpha\text{-}\beta}$. For the same reason, only the Ca-free data within $M_{En}/(M_{En} + M_{Fs})$ = 70–100% are considered when we investigate the effects of variation of M_{MgTs} on $P_{\beta\text{-}\gamma}$, since the compositional variation of En-Fs remarkably influences $P_{\beta\text{-}\gamma}$ (Figure 2a). The results indicate that increasing M_{MgTs} remarkably increases the $P_{\beta\text{-}\gamma}$ (Figure 2b), as indicated by the linear regression equation: $P_{\beta\text{-}\gamma}$ (GPa) = 26.3(1) + 0.38(9)M_{MgTs}, and R^2 = 0.89.

The incorporation of Ca influences the $P_{\alpha\text{-}\beta}$ and $P_{\beta\text{-}\gamma}$. The $P_{\alpha\text{-}\beta}$ of Ca-bearing orthopyroxenes are higher than those of Al-bearing Ca-free orthopyroxenes (Figure 2a), while Ca-bearing orthopyroxenes have a lower $P_{\beta\text{-}\gamma}$ (Figure 2b). However, the limited amount of data and range of variation of the Ca content do not suffice for quantitative analysis.

In summary, when M_{En} = 40–100, within the En-Fs-MgTs, the compositional variation only weakly influences the $P_{\alpha\text{-}\beta}$, and increasing M_{En} and M_{MgTs} remarkably increase the $P_{\beta\text{-}\gamma}$. In addition, the incorporation of Ca observably increases the $P_{\alpha\text{-}\beta}$ and decreased the $P_{\beta\text{-}\gamma}$.

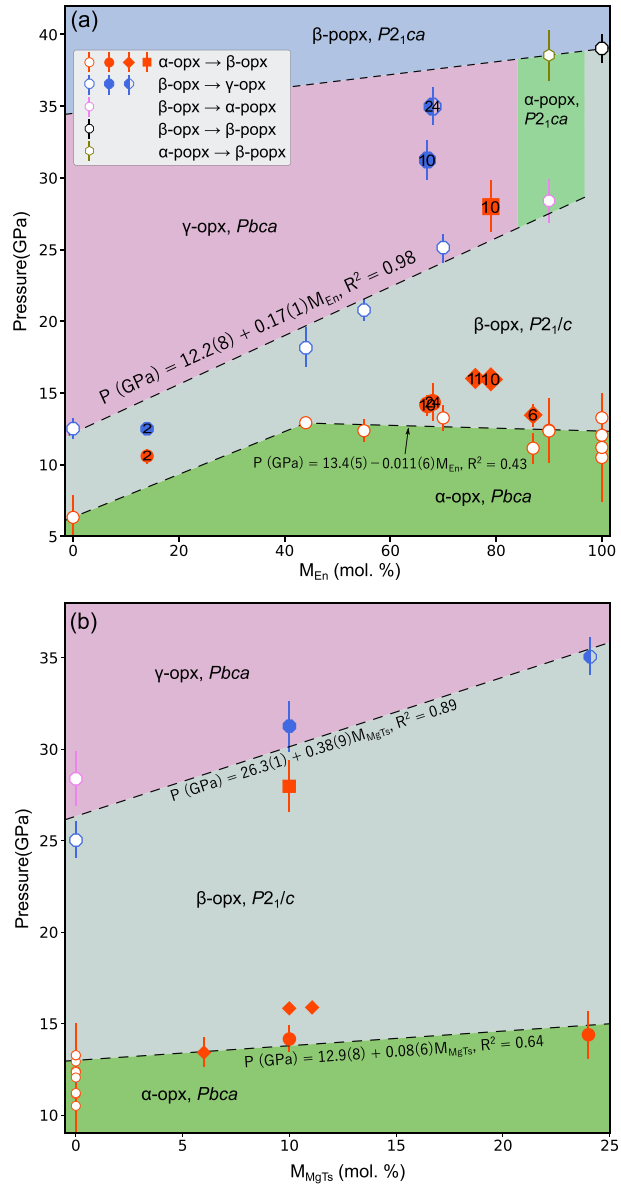

Figure 2. Phase transitions of Mg-Fe-Al orthopyroxene at room-*T* in the pressure-composition space, showing how the phase-transition pressure changes with M_{En} (a) and M_{MgTs} (b). The symbols represent experimentally determined pressures of phase transitions, including α-opx → β-opx, β-opx → γ-opx, β-opx → α-popx, β-opx → β-popx, and α-popx → β-popx. The hollow and solid symbols represent Al-free and Al-bearing orthopyroxenes, respectively, within the En-Fs join. The half-filled hexagon indicates that the phase transition was not observed at the highest pressure. The square and diamond symbols represent Ca-bearing orthopyroxenes. The Al content of each Al-bearing orthopyroxene is signified by the M_{MgTs} value written on the symbol in (a). The shaded areas indicate the regions of different phases, including α-opx, β-opx, α-popx, γ-opx, and β-popx. The space group of each phase is also shown. In (a), the dashed lines represent weighted regressions of the data (*P*-M_{En}) for the phase transitions, and only Al- and Ca-free data are considered. The regression equation of each dashed line is shown nearby. The *P*- M_{En} data for the α-opx → β-opx phase transition are split into two pieces (M_{En} = 0–44 and M_{En} = 44–100) for linear regression since the data follow different linear trends over different regions of the data, and the end-member En is excluded as the scattered results from different measurements lead to unreasonable fitting. In (b), the dashed lines represent weighted regressions of the data (*P* - M_{MgTs}) for the phase transitions, and only Ca-free orthopyroxenes are included. Error bars smaller than the symbol size are not shown. The data used are from this study and previous studies (Dera, Finkelstein, et al., 2013; Finkelstein et al., 2015; Lin et al., 2005; Serghiou et al., 2000; Xu et al., 2020; Xu et al., 2018; Zhang, Jackson, et al., 2013; Zhang et al., 2012; Zhang, Reynard, et al., 2013), which are also available in Table S5 in the Supporting Information S1.

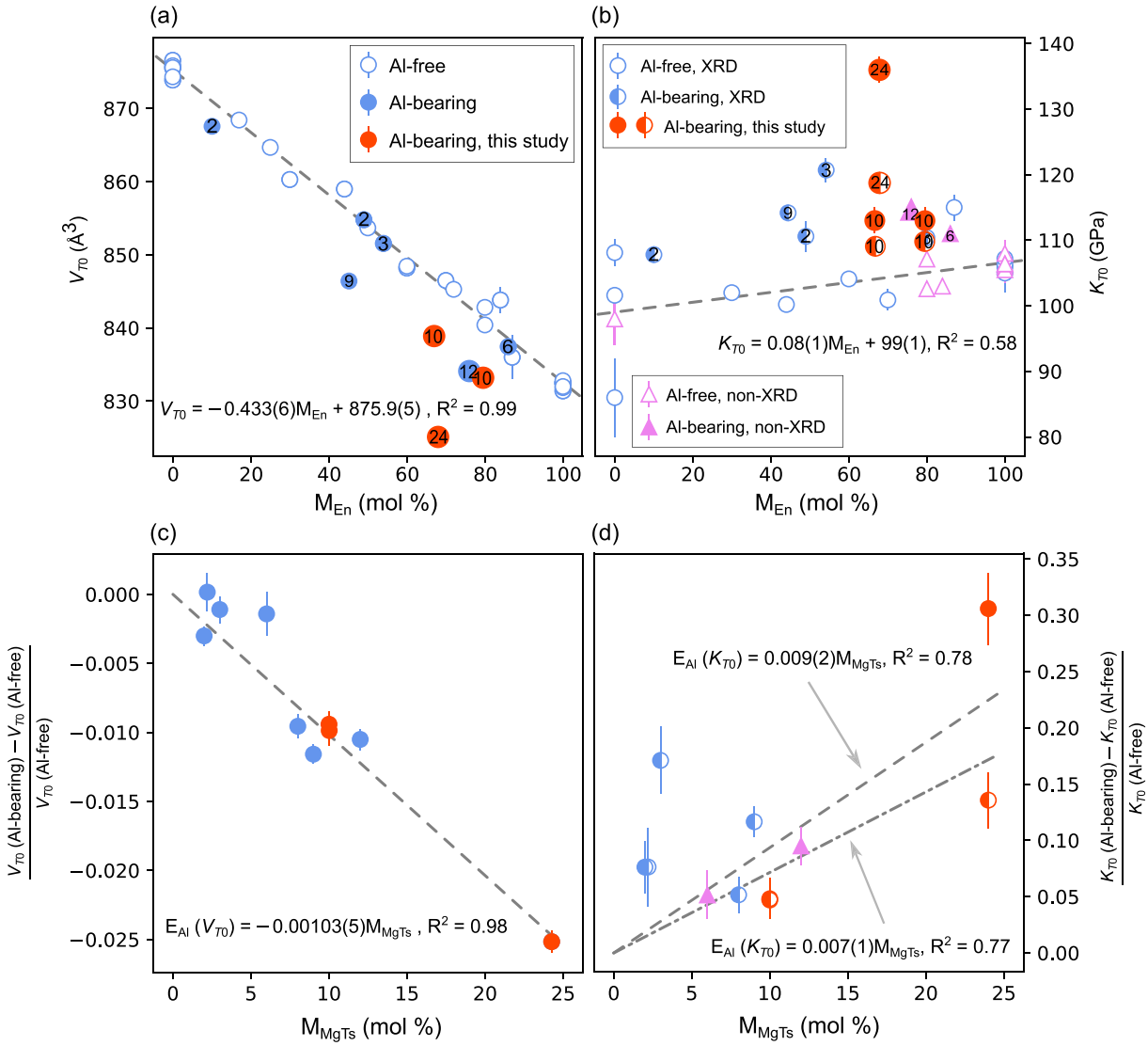

Figure 3. (a) Zero-pressure volume (V_{T0}) and (b) Isothermal bulk modulus (K_{T0}) of Mg-Fe-Al orthopyroxenes at zero pressure as a function of M_{En}. (c) and (d) present the effects of Al on the V_{T0} (E_{Al} (V_{T0})) and K_{T0} (E_{Al} (K_{T0})) of orthopyroxene as a function of the M_{MgTs} content defined by [V_{T0} (Al-bearing) – V_{T0} (Al-free)]/V_{T0} (Al-free) and [K_{T0} (Al-bearing) – K_{T0} (Al-free)]/K_{T0} (Al-free), respectively. The hollow and solid symbols in (a) and (b) represent Al-free and Al-bearing orthopyroxenes, respectively. In (a) and (b), the Al content of each Al-bearing orthopyroxene is denoted by the corresponding M_{MgTs} value written on the symbol. The blue and violet symbols represent results from previous studies, while the red symbols represent those from this study. In (b) and (d), the circular and triangular symbols represent values derived from XRD and non-XRD methods (e.g., BS, UI), respectively. The K_{T0} determined by XRD in previous studies was obtained by refitting the data to the BM3 EoS with fixed $K'_{T0} = 8$. The red and red half-filled symbols (this study) represent values obtained by fitting the data to the BM3 EoS with and without fixed $K'_{T0} = 8$, respectively. The dashed lines in (a) and (b) represent linear fitting of the Al-free data, while the dashed lines in (c) and (d) represent linear fitting of all the data with fixed y-intercept (0). In (d), the dash-dotted line represents linear fitting of all the data including the XRD data whose K_{T0} values are obtained with fixed $K'_{T0} = 8.0$; while in the dashed-line linear fitting, the K_{T0} of the data point ($M_{MgTs} = 24$) obtained without fixed $K'_{T0} = 8$ instead of that obtained with fixed $K'_{T0} = 8$ is included. The formula of each line is shown in each subplot. The adiabatic bulk moduli (K_{S0}) obtained by non-XRD methods are converted to their corresponding isothermal values (K_{T0}) using the following equation: $K_{T0} = K_{S0}/(1 + \alpha\gamma T)$, where α is thermal expansion coefficient, γ is the Grüneisen parameter (Yang & Ghose, 1994), and T is temperature. Error bars smaller than the symbol size are not shown. The data used in this figure are available in Table S6 in the Supporting Information S1.

4.2. Effects of Temperature on the Phase Transitions of Orthopyroxene

Zhang et al. (2014) performed Raman spectroscopy experiments on orthopyroxenes at high P-T up to 18.2 GPa and 673 K, and the results suggested that temperature has almost no effect on the $P_{\alpha\text{-}\beta}$ ($dP_{\alpha\text{-}\beta}/dT = 0$). In this study, the effect of temperature on the α-opx → β-opx phase transition of $En_{67}Fs_{23}MgTs_{10}$ and $En_{68}Fs_8MgTs_{24}$ was vague due to the large pressure steps, but the $En_{79}Fs_9MgTs_{10}Wo_2$ data collected at room-T high-P and high

P-T were consistent with a zero $dP_{\alpha\text{-}\beta}/dT$ (Figures 1 and S5 in the Supporting Information S1). In contrast, high *T* significantly decreased the $P_{\beta\text{-}\gamma}$. The $P_{\beta\text{-}\gamma}$ of $En_{79}Fs_9MgTs_{10}Wo_2$ was 29.7 GPa at room-*T*, which is larger than the $P_{\beta\text{-}\gamma}$ at 700 K (25.0 GPa); The $P_{\beta\text{-}\gamma}$ of $En_{67}Fs_{23}MgTs_{10}$ was 32.6 GPa at 300 K, and it was 24.4 GPa at 700 K. The β-opx → γ-opx phase transition of $En_{68}Fs_8MgTs_{24}$ was not observed at high *P* up to the maximum pressure of 35.1 GPa, but this phase transition occurred at 29.5 GPa at 700 K. Moreover, at high *T* the $P_{\beta\text{-}\gamma}$ of $En_{68}Fs_8MgTs_{24}$ is ~5 GPa larger than those of $En_{67}Fs_{23}MgTs_{10}$ and $En_{79}Fs_9MgTs_{10}Wo_2$ (~25 GPa). Therefore, the $P_{\beta\text{-}\gamma}$ at high *T* also increases with increasing Al content (Figures 1 and S5 in the Supporting Information S1).

4.3. Compositional Effects on the EoS of Orthopyroxene

To investigate the compositional effects on the EoS of orthopyroxene, we compared the thermal EoS parameters (V_{T0}, K_{T0}, α_{300}, and $(\partial K_T/\partial T)_P$) of orthopyroxenes with various compositions from this study and from previous studies (Bass & Weidner, 1984; Chai et al., 1997; de Vries et al., 2013; Dera, Finkelstein, et al., 2013; Dietrich & Arndt, 1982; Flesch et al., 1998; Frisillo & Barsch, 1972; Frisillo & Buljan, 1972; Hugh-Jones, 1997; Hugh-Jones et al., 1997; Hugh-Jones & Angel, 1994; Hugh-Jones & Angel, 1997; Jackson et al., 2003; Jackson et al., 1999; Jackson et al., 2007; Kumazawa, 1969; Kung et al., 2004; Nestola et al., 2008; Periotto et al., 2012; Sarver & Hummel, 1962; Saxena, 1988; Scandolo et al., 2015; Sueno et al., 1976; Webb & Jackson, 1993; Weidner et al., 1978; Xu et al., 2016; Xu et al., 2018; Xu et al., 2020; Xu, Ma, et al., 2017; Yang & Ghose, 1994; Zhao et al., 1995; Zhang & Bass, 2016; Zhang, Jackson, et al., 2013). Due to the trade-off between K_{T0} and K'_{T0}, the thermal EoS parameters derived by XRD method were redetermined by refitting the data to BM3 EoS with fixed $K'_{T0} = 8$, which is very close to the K'_{T0} of En (Angel & Jackson, 2002; Periotto et al., 2012; Xu et al., 2018). In addition, the adiabatic bulk moduli (K_{S0}) and their temperature derivative ($(\partial K_S/\partial T)_P$) obtained by methods other than XRD (e.g., BS and UI) were converted to their corresponding isothermal values (K_{T0} and $(\partial K_T/\partial T)_P$) using the following equations: $K_{T0} = K_{S0}/(1 + \alpha\gamma T)$ and $(\partial K_S/\partial T)_P = (\partial K_T/\partial T)_P + \alpha\gamma T/(1 + \alpha\gamma T)$, where α is thermal expansion coefficient, γ is Grüneisen parameter (Yang & Ghose, 1994), and *T* is temperature. The results are summarized in Figure 3 and Table S6 in the Supporting Information S1.

For the En-Fs orthopyroxenes, the V_{T0} decreases monotonically with increasing En, as suggested by Tarantino et al. (2002) and shown in Figure 3a. A weighted linear regression of the En-Fs data yields the following equation: $V_{T0} = -0.433(3)M_{En} + 875.9(5)$, $R^2 = 0.99$. The incorporation of Al significantly decreases the V_{T0}, as shown in Figure 3a, and the V_{T0} of the Al-bearing orthopyroxenes is smaller than those of their adjacent Al-free orthopyroxenes. For instance, the V_{T0} of $En_{67}Fs_{23}MgTs_{10}$ and $En_{68}Fs_8MgTs_{24}$ is 0.9% and 2.5% lower than that of $En_{67}Fs_{33}$ within the En-Fs join. The K_{T0} of En-Fs orthopyroxene increases with increasing M_{En} (Figure 3b), which can be described by the linear regression equation: $K_{T0} = 0.08(1)M_{En} + 99(1)$, $R^2 = 0.58$. In addition to influencing the V_{T0}, the incorporation of Al also influences the K_{T0} of orthopyroxene. As shown in Figure 3b, Al-bearing orthopyroxenes have larger K_{T0} than Al-free orthopyroxenes. The exception is $En_{87}Fs_{13}$ obtained by Zhang, Jackson, et al. (2013), which has a significantly larger K_{T0} than the other En-Fs orthopyroxenes (Figure 3b).

In this study, fitting the *P-V-T* data to the BM3 EoS yielded $K_{T0} = 113.0(20)$ GPa and $K'_{T0} = 7.1(4)$ for $En_{79}Fs_9MgTs_{10}Wo_2$, and $K_{T0} = 113.0(20)$ GPa and $K'_{T0} = 7.0(5)$ for $En_{67}Fs_{23}MgTs_{10}$; with fixed $K'_{T0} = 8$, the K_{T0} was determined to be 109.9(6) and 109.1(6) GPa for $En_{79}Fs_9MgTs_{10}Wo_2$ and $En_{67}Fs_{23}MgTs_{10}$, respectively. However, the BM3 EoS fitting yields $K_{T0} = 136.0(20)$ GPa and $K'_{T0} = 3.5(5)$ for $En_{68}Fs_8MgTs_{24}$ without any constraint. It should be noted that the $K_{T0} = 136.0(20)$ GPa obtained for $En_{68}Fs_8MgTs_{24}$ is significantly (~20%) larger than those of $En_{79}Fs_9MgTs_{10}Wo_2$ and $En_{67}Fs_{23}MgTs_{10}$, and it is the highest K_{T0} of orthopyroxene obtained thus far.

Unlike other upper mantle minerals (olivine, clinopyroxene, and garnet) whose K'_{T0} are around 4 (e.g., Downs et al., 1996; Sinogeikin & Bass, 2000; Xu, Zhang, et al., 2017), orthopyroxene has "anomalously" high value of K'_{T0}, such as $K'_{T0} = \sim 8$ for En (Angel & Jackson, 2002). In this study, the obtained K'_{T0} for $En_{79}Fs_9MgTs_{10}Wo_2$ and $En_{67}Fs_{23}MgTs_{10}$ are consistent with the values of K'_{T0} reported by previous studies on orthopyroxene (e.g., Angel & Jackson, 2002; Chai et al., 1997; Zhang & Bass, 2016). In contrast, the obtained $K'_{T0} = 3.5(5)$ for $En_{68}Fs_8MgTs_{24}$ is much smaller. Therefore, it should be cautious with such a small K'_{T0}. We compared the EoS fits without constraint on K'_{T0} and with fixed $K'_{T0} = 8$ for the three orthopyroxenes. As shown in Figures S6a and S6b in the Supporting Information S1, for $En_{79}Fs_9MgTs_{10}Wo_2$ and $En_{67}Fs_{23}MgTs_{10}$, the EoS fit that has K'_{T0} fixed at 8 is very consistent with the EoS fit that has no constraint on K'_{T0}, indicating that K'_{T0} is very close to 8 for these two orthopyroxenes. However, for $En_{68}Fs_8MgTs_{24}$, the EoS fit that has K'_{T0} fixed at 8 significantly increases the misfit to the data in comparison to the EoS fit that has no constraint on K'_{T0} (Figure S6c in the

Supporting Information S1). In addition, the f_E-F_E plot (Angel, 2000) was used to assess the quality of the EoS fit. As shown in Figure S7a and S7b in the Supporting Information S1, the f_E-F_E data lie on an inclined line for $En_{79}Fs_9MgTs_{10}Wo_2$ and $En_{67}Fs_{23}MgTs_{10}$, and either the EoS fit that has K'_{T0} fixed at 8 or the EoS fit that has no constraint on K'_{T0} represents the f_E-F_E data very well. For $En_{68}Fs_8MgTs_{24}$, however, the EoS fit that has K'_{T0} fixed at 8 does not represent the f_E-F_E data (Figure S7c in the Supporting Information S1); and the f_E-F_E data almost lie on a nearly horizontal line, indicating that the K'_{T0} is very close to 4 (Angel, 2000).

Moreover, fitting the *P-V-T* data to the BM3 EoS with/without fixed $K'_{T0} = 8$ yielded reasonable values of α_T and $(\partial K_T/\partial T)_P$ for $En_{79}Fs_9MgTs_{10}Wo_2$ and $En_{67}Fs_{23}MgTs_{10}$ (Figure S8 and Table S6 in the Supporting Information S1). However, with fixed $K'_{T0} = 8$, the EoS fitting yielded α_T and $(\partial K_T/\partial T)_P$ with very large uncertainties (Figure S8 and Table S6 in the Supporting Information S1), also indicating that, unlike $En_{79}Fs_9MgTs_{10}Wo_2$ and $En_{67}Fs_{23}MgTs_{10}$, $En_{68}Fs_8MgTs_{24}$ has a K'_{T0} significantly deviating from 8.

Due to the trade-off between K_{T0} and K'_{T0} when performing an EoS fit, the obtained high/low value of K_{T0}/K'_{T0} of $En_{68}Fs_8MgTs_{24}$ still needs confirmation from direct measurements of the elastic constants. However, our EoS fits of $En_{79}Fs_9MgTs_{10}Wo_2$ and $En_{67}Fs_{23}MgTs_{10}$ yield values of K_{T0} that are comparable to the values of orthopyroxenes that contain comparable Al contents obtained by direct measurements (Table S6 in the Supporting Information S1). Thus, the BM3 EoS fitting of our data can yield reliable values of K_{T0}. The volume data of $En_{68}Fs_8MgTs_{24}$ were collected using the same method as that was used for the other two orthopyroxenes, the obtained K_{T0} should also be comparable to that obtained by direct measurement. The obtained high/low value of K_{T0}/K'_{T0} of $En_{68}Fs_8MgTs_{24}$ is therefore unlikely the result of experimental artifacts but likely caused by the extremely high Al content. Such a high K_{T0} can be explained by the high Al content because tetrahedral Al substitutes Si and stiffens the orthopyroxene structure (e.g., Chai et al., 1997; Xu et al., 2016). In addition, for isostructural minerals, the bulk modulus normally increases with decreasing unit-cell volume (e.g., Gao et al., 2014), and the incorporation of ~12 wt. % Al_2O_3 lowers the unit-cell volume of $En_{68}Fs_8MgTs_{24}$ by 2.5% in comparison with Al-free orthopyroxene (Figure 3a). Moreover, the low value of K'_{T0} indicates that, when the Al content incorporated in orthopyroxene is as high as that in $En_{68}Fs_8MgTs_{24}$, the incorporation of Al may change the compression mechanism of orthopyroxene.

To quantitatively describe the effect of Al on V_{T0}, we defined $E_{Al}(V_{T0}) = [V_{T0}\text{ (Al-bearing)} - V_{T0}\text{ (Al-free)}]/V_{T0}$ (Al-free) to evaluate the effect of Al incorporation on the V_{T0}, and $E_{Al}(K_{T0}) = [K_{T0}\text{ (Al-bearing)} - K_{T0}\text{ (Al-free)}]/K_{T0}$ (Al-free) was defined in the same way. This relation highlights how the variation in Al content (M_{MgTs}) influences V_{T0} and K_{T0} (Figures 3c and 3d). As shown in Figure 3c, the $E_{Al}(V_{T0})$ decreases with increasing M_{MgTs}, as described by the linear regression equation $E_{Al}(V_{T0}) = -0.00103(5)M_{MgTs}$, $R^2 = 0.98$. The $E_{Al}(K_{T0})$ increases with increasing M_{MgTs} (Figure 3d), as indicated by the linear regression equation $E_{Al}(K_{T0}) = 0.007(1)M_{MgTs}$, $R^2 = 0.77$, when performing the linear fitting of all the data including the XRD data whose K_{T0} values are obtained with fixed $K'_{T0} = 8.0$; or $E_{Al}(K_{T0}) = 0.009(2)M_{MgTs}$, $R^2 = 0.78$, when the K_{T0} of the data point ($M_{MgTs} = 24$) obtained without fixed $K'_{T0} = 8$ instead of that obtained with fixed $K'_{T0} = 8$ is included in the linear fitting.

In contrast to V_{T0} and K_{T0}, the compositional effects on α_{300} are indistinct. As shown in Figure S5a and Table S6 in the Supporting Information S1, the obtained values of α_{300} for $En_{79}Fs_9MgTs_{10}Wo_2$, $En_{67}Fs_{23}MgTs_{10}$, and $En_{68}Fs_8MgTs_{24}$ in this study are very close to each other, within the uncertainty. These values are very similar to those of En (Hugh-Jones, 1997; Jackson et al., 2003; Zhao et al., 1995). Similarly, the $(\partial K_T/\partial T)_P$ of the various orthopyroxenes are comparable within the uncertainty (Figure S5a in the Supporting Information S1). The $(\partial K_T/\partial T)_P$ of $En_{79}Fs_9MgTs_{10}Wo_2$, $En_{67}Fs_{23}MgTs_{10}$, and $En_{68}Fs_8MgTs_{24}$ are within −0.031(9) - −0.016(12) GPa/K.

5. Geophysical Implications

Previous studies suggested that the pressure-induced phase transition of orthopyroxene depends on the temperature. Orthopyroxene transforms into high-*P* clinopyroxene (hpcpx) at ~7 GPa, and the pressure of this transition increases with increasing temperature (Akashi et al., 2009; Fei et al., 1990; Ito & Navrotsky, 1985; Ono et al., 2018). This phase transition requires high temperatures of ~1000 K (Akashi et al., 2009; Woodland, 1998). With increasing pressure, hpcpx either transforms into majorite at very high *T* (>1800 K) or decomposes into wadsleyite and stishovite at relatively low *T* (<1800 K; Fei et al., 1990; Ito & Navrotsky, 1985; Ono et al., 2018).

High *P-T* experiments at temperatures lower than 800 K have shown metastable phase transitions of orthopyroxene. Several studies (Xu et al., 2018, 2020; Zhang et al., 2014) have shown that the pressure-induced α-opx → β-opx and β-opx → γ-opx phase transitions apply to En-Fs orthopyroxenes with $M_{En} \leq 70$ under relatively low temperatures (≤800 K). In this study, room-*T* high-*P* experiments have demonstrated the α-opx → β-opx phase transition in synthetic $En_{67}Fs_{23}MgTs_{10}$, $En_{68}Fs_8MgTs_{24}$ and natural $En_{79}Fs_9MgTs_{10}Wo_2$, and we have observed the β-opx → γ-opx phase transition in $En_{67}Fs_{23}MgTs_{10}$ and $En_{79}Fs_9MgTs_{10}Wo_2$ (Figures 1 and 2). The high *P-T* experiments showed that $En_{79}Fs_9MgTs_{10}Wo_2$, synthetic $En_{67}Fs_{23}MgTs_{10}$ and $En_{68}Fs_8MgTs_{24}$ undergo stepwise α-opx → β-opx → γ-opx phase transitions with increasing pressure and temperature up to ~30 GPa and 700 K (Figures 1 and S5 in the Supporting Information S1). Our experiments indicate that α-opx → β-opx → γ-opx phase transitions occur in Mg-Fe-Al-Ca orthopyroxenes at high *P-T*, even when the Al content is extremely high (~12 wt. % Al_2O_3 in $En_{68}Fs_8MgTs_{24}$), and the variation in composition shifts the pressures of the phase transitions, especially for the β-opx → γ-opx phase transition (Figures 1 and 2). In natural orthopyroxenes, Mg^{2+}, $Fe^{2+,}$ and Al^{3+} are the most abundant cations other than Si^{4+}, and Ca^{2+} usually occurs as a very minor component, as in San Carlos $En_{79}Fs_9MgTs_{10}Wo_2$ in this study. Therefore, this study indicates that the stepwise α-opx → β-opx → γ-opx phase transitions exist for most natural orthopyroxenes under relatively low temperatures.

Among various geological settings, the subduction zone at the convergent plate boundary is the most likely place where the α-opx → β-opx → γ-opx phase transitions occur for orthopyroxenes. Under such conditions, the old and fast subducting slabs bear low-*T* conditions in the slab center (harzburgite layer) and thus enable a metastable region that possesses untransformed phases that do not exist under the normal mantle geotherms (e.g., Faccenda & Dal Zilio, 2017; Kirby et al., 1996). The metastable region is regarded as one of the key factors that cause the presence of stagnant slabs at the transition zone in some subduction zones, and the temperature of the slab center is estimated to be lower than 1000 K in some cases (e.g., Ganguly et al., 2009; King et al., 2015). Under such conditions, the dissolution of pyroxene in garnet could be inhibited in geological time scales (Nishi et al., 2013; Van Mierlo et al., 2013).

The α-opx → β-opx and β-opx → γ-opx transition are displacive phase transitions (Dera, Finkelstein, et al., 2013) as indicated by the group-subgroup relation of their space group (*Pbca* and $P2_1/c$) and their similar structure topology, indicating that the atomic displacements through the phase transitions are small (Dove, 1997). Displacive phase transitions have very low activation energies and usually can occur at room-*T* (Shekar & Rajan, 2001) in a matter of seconds, or shorter. In this study, we observed the α-opx → β-opx and β-opx → γ-opx transition both at room-*T* and high-*T*. In the experiment, the high *P-T* condition was kept for about 1 hr, and the phase transition occurred rapidly within the first few minutes. Therefore, the α-opx → β-opx and β-opx → γ-opx transition are much more likely to occur under cold slab conditions in comparison to the dissolution of pyroxene in garnet which is largely diffusion-controlled (Nishi et al., 2013; Van Mierlo et al., 2013).

The high *P-T* experiments in this study provide insights into the possible metastable phases of orthopyroxene preserved within such cold stagnant slabs (Figure 4). The α-opx → β-opx → γ-opx phase transitions occur as the slabs undergo downwelling. The variations in the contents of Fe and Al do not significantly change the depth of the α-opx → β-opx transition but significantly shift the boundary between the β-opx and γ-opx in the opposite direction. In addition, the incorporation of Ca deepens the α-opx → β-opx transition and shallows the β-opx → γ-opx phase transition. Therefore, the β-opx and γ-opx could be the possible metastable phases of orthopyroxenes within the stagnant slabs that locate at the transition zone (Figure 4).

We have modeled the densities of these three orthopyroxenes (α-opx, β-opx, and γ-opx) as well as the subduction slab and the surrounding mantle (Figure 4b) along the cold slab geotherm using the measured thermal EoS parameters. The density of the γ-opx phase is assumed to be 2% larger than that of β-opx and has the same thermal EoS parameters as β-opx due to the lack of thermal EoS parameters. For the modeling of the slab density profile, we adopt the slab model proposed by Ringwood (1982) which is ~80 km thick and composed of from top to bottom a basalt layer (6.5 km thick), a 23.5-km thick residual harzburgite layer, a residual lherzolite (10 km thick), and a depleted pyrolite layer (40 km thick). The major element bulk chemistries of the different layers include a MORB (mid-ocean ridge basalt) composition (Sanehira et al., 2008) for the top basalt layer, an ophiolitic harzburgite (Tamura & Arai, 2006) for the residual harzburgite layer, and a depleted mantle composition (Workman & Hart, 2005) for the residual lherzolite and the depleted pyrolite layers as the minor difference between these two lithological units does not affect the density structure (Ganguly et al., 2009). The mantle composition is represented by the pyrolite model (Green, 1979). The mineral proportions and mineral compositions of the MORB,

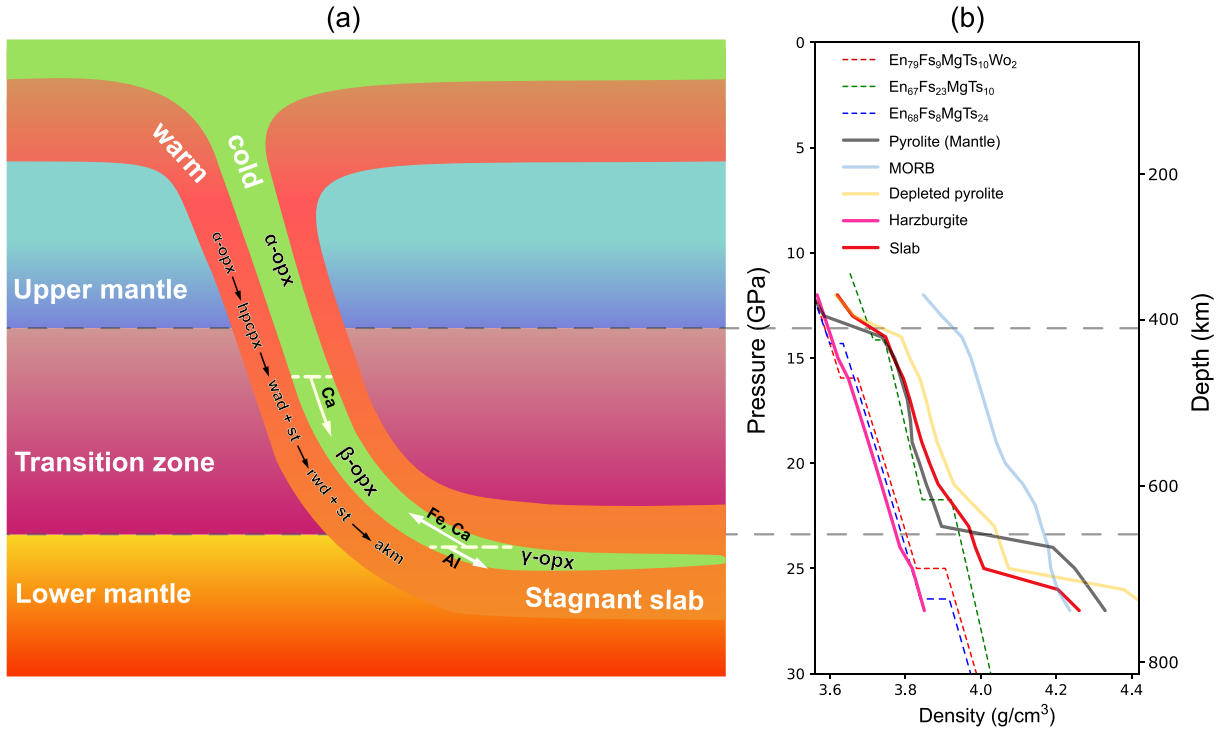

Figure 4. (a) A schematic diagram of a cold subducting slab, showing the metastable phase transitions of orthopyroxene (α-opx → β-opx → γ-opx) in the cold regions of the slab, in comparison with the α-opx → hpcpx → wad + stv → rwd + stv → akm transition (hpcpx = high-pressure clinopyroxene; wad = wadsleyite; stv = stishovite; rwd = ringwoodite; akm = akimotoite) under higher temperature conditions (Ono et al., 2018). The variations in Fe and Al contents do not significantly influence the pressure of the α-opx → β-opx transition but significantly shift the boundary between the β-opx and γ-opx in the opposite direction; the addition of Ca increases the pressure of the α-opx → β-opx transition but decreases the pressure of the β-opx → γ-opx transition. (b) Densities of three orthopyroxenes ($En_{79}Fs_9MgTs_{10}Wo_2$, $En_{67}Fs_{23}MgTs_{10}$, and $En_{68}Fs_8MgTs_{24}$ represented by red, green, and blue dashed lines, respectively) in comparison with the densities of different lithological units of the slab, the entire slab, and the pyrolite mantle. The MORB, harzburgite, depleted pyrolite, the entire slab and the pyrolite mantle are represented by light blue, magenta, yellow, red, and black solid lines, respectively.

depleted pyrolite, and pyrolite as functions of *P* along the geotherms (Ganguly et al., 2009) are calculated using the Perple_X software package (Connolly, 2005). The obtained mineral proportions and mineral compositions are reported in Figure S9 and Tables S7–S9 in the Supporting Information S1. The mineral proportions and compositions of the harzburgite are not calculated but adopted from Tamura and Arai (2006), which is composed of 78 vol. % olivine ($Mg_{1.8}F_{0.2}SiO_4$) and 22 vol. % orthopyroxene ($En_{87}Fs_9MgTs_2Wo_2$). The olivine and orthopyroxene in the harzburgite are assumed to be metastable phases as olivine is also considered to be metastable under the cold subduction zone condition (e.g., Ishii & Ohtani, 2021). The mineral proportions and compositions are assumed to be constant. The α-opx → β-opx and β-opx → γ-opx transition of orthopyroxene are included in the harzburgite.

The density of each mineral at varying *P-T* is calculated using the thermal EoS parameters summarized in Table S10 in the Supporting Information S1 (Text S1 in the Supporting Information S1; Arimoto et al., 2015; Armentrout & Kavner, 2011; Downs et al., 1996; Fan et al., 2019; Gréaux et al., 2011; Horiuchi et al., 1987; Jephcoat et al., 1999; Katsura et al., 2009; Liu et al., 1999; Liu & Li, 2006; Mao et al., 2011; Nishihara et al., 2004; Reichmann et al., 2002; Ricolleau et al., 2009; Shinmei et al., 1999; Sinogeikin & Bass, 2002; Tribaudino & Mantovani, 2014; Wang et al., 2014; Zhang et al., 1997; Zhao et al., 1998; Zhao et al., 1995; Zhao et al., 1997; Zou et al., 2012). The density of each lithological unit is calculated using the Voigt-Reuss-Hill average scheme.

The densities of different lithological units of the slab are compared in Figure 4b with the pyrolite mantle density. As shown in Figure 4b, the densities of the basalt and depleted pyrolite layers are higher than the mantle density in the upper mantle and in the deepest range of the transition zone, which is consistent with the results reported by Ganguly et al. (2009). This is reasonable as the basalt layer is mainly composed of garnet, stishovite, and clinopyroxene, and with increasing pressure, the volume of the low-density clinopyroxene is diminishing, while the amount of dense garnet is increasing (Figure S9 in the Supporting Information S1). The depleted pyrolite and

the pyrolite mantle are very similar in mineral species (Figure S9 in the Supporting Information S1), the higher density of the former is attributed to its lower temperature in comparison to the latter (Ganguly et al., 2009). However, at the bottom of the transition zone, as ringwoodite decomposes into bridgmanite and magnesiowüstite (rwd → bdg + mw) under mantle geotherm, the density of the depleted pyrolite is less than the density of the pyrolite mantle which jumps by 6.7% while the rwd → bdg + mw transition in the former is postponed due to the low *T* in the slab (Faccenda & Dal Zilio, 2017).

The density of the harzburgite layer is slightly higher than the mantle density in the upper mantle although the harzburgite does not contain the densest silicate mineral in the upper mantle (garnet), and the higher density of the former is attributed to its low temperature. However, in the transition zone, the harzburgite is much (up to 4.2%) less dense than the pyrolite mantle, indicating that the temperature effect on the density is minor in comparison to the effects of mineral species. The density increases of the harzburgite contributed by the metastable phase transitions of orthopyroxene are very limited. As shown in Figure 4b, the α-opx → β-opx and β-opx → γ-opx transition increase the density of harzburgite by 0.3% and 0.4% at 16 and 25 GPa, respectively, although these phase transitions result in 1.2%–2.0% density increase of orthopyroxene. Therefore, the density increase by the metastable phase transitions of orthopyroxene is negligible in comparison to the density contrast between the harzburgite and the pyrolite mantle.

The density of the entire slab is also shown in Figure 4b, which is up to 2.1% higher than the pyrolite mantle density in the upper mantle. At the upper region of the transition zone (410–500 km) the densities of the slab and the pyrolite mantle become very comparable, then the density contrast (up to 1.8%) increases with increasing depth in the lower region of the transition zone. At the bottom of the transition zone where the rwd → bdg + mw transition largely increases the pyrolite mantle density; thus, the slab becomes 4.9% less dense than the pyrolite mantle. Therefore, our slab modeling shows that the metastable olivine and orthopyroxene in the harzburgite layer and the postponed rwd → bdg + mw transition in the depleted pyrolite layer would cause the cold subducted plate much less dense than the surrounding mantle and promote the stagnation of the slab at the bottom of the transition zone. Previous studies have shown that the postponed rwd → bdg + mw transition in the slab would cause the slab stagnation at the bottom of the transition zone (e.g., Faccenda & Dal Zilio, 2017). In this study, our results indicate that the existence of metastable orthopyroxene and olivine in the harzburgite layer would be another contribution to the slab stagnation at the bottom of the transition zone in addition to the postponed rwd → bdg + mw transition. In addition, our results show that the slab and the mantle are very close in density in the upper region of the transition zone. This indicates that the existence of a large amount of metastable olivine and orthopyroxene in the harzburgite layer could cause slab stagnation in the upper region of the transition zone, which could be related to stagnant slabs that are well above the 660-km discontinuity in some subduction zones such as the stagnant slabs in the Bonin arc and southern Kurile arc (Fukao & Obayashi, 2013).

Conflict of Interest

The authors declare no conflicts of interest relevant to this study.

Data Availability Statement

Per AGU's Data Policy, the supporting data have been deposited in a general repository, Zenodo, https://doi.org/10.5281/zenodo.3613769.

References

Agrusta, R., Hunen, J., & Goes, S. (2014). The effect of metastable pyroxene on the slab dynamics. *Geophysical Research Letters*, *41*, 8800–8808. https://doi.org/10.1002/2014gl062159

Akashi, A., Nishihara, Y., Takahashi, E., Nakajima, Y., Tange, Y., & Funakoshi, K. i. (2009). Orthoenstatite/clinoenstatite phase transformation in $MgSiO_3$ at high-pressure and high-temperature determined by in situ X-ray diffraction: Implications for nature of the X discontinuity. *Journal of Geophysical Research*, *114*, B04206. https://doi.org/10.1029/2008JB005894

Angel, R. J. (2000). Equations of state. *Reviews in Mineralogy and Geochemistry*, *41*(1), 35–59. https://doi.org/10.2138/rmg.2000.41.2

Angel, R. J., & Jackson, J. M. (2002). Elasticity and equation of state of orthoenstatite, $MgSiO_3$. *American Mineralogist*, *87*(4), 558–561. https://doi.org/10.2138/am-2002-0419

Arai, S., & Abe, N. (1995). Reaction of orthopyroxene in peridotite xenoliths with alkali-basalt melt and its implication for genesis of alpine-type chromitite. *American Mineralogist*, *80*(9–10), 1041–1047. https://doi.org/10.2138/am-1995-9-1020

Acknowledgments
This work is supported by the National Natural Science Foundation of China (42172048, 41802043, and U2032118), the Youth Innovation Promotion Association CAS (2018434), the Chinese Academy of Sciences "Light of West China" Program (2019), the Science and Technology Foundation of Guizhou Province (QKHJC-ZK[2021]ZD042), and the Innovation and Entrepreneurship Funding of High-Level Overseas Talents of Guizhou Province ([2019]10). The authors thank Vitali B. Prakapenka for his help in the experiments at 13-BM-D. The diffraction experiments were performed at GeoSoilEnviroCARS (Sector13-BM-C and BM-D), Partnership for Extreme Crystallography program (PX^2), Advanced Photon Source (APS), and Argonne National Laboratory. GeoSoilEnviroCARS is supported by the National Science Foundation—Earth Sciences (EAR-1634415) and the Department of Energy—Geosciences (DE-FG02-94ER14466). PX^2 program is supported by COMPRES under NSF Cooperative Agreement EAR-1661511. The use of the COMPRES-GSECARS gas loading system was supported by COMPRES under NSF Cooperative Agreement EAR-1661511 and by GSECARS. Use of the APS was supported by the U.S. Department of Energy, Office of Science, Office of Basic Energy Sciences, under Contract No. DE-AC02-06CH11357. We thank the editor for handling this manuscript, and the associate editor and two reviewers for constructive suggestions and comments which helped to improve the manuscript.

Arimoto, T., Gréaux, S., Irifune, T., Zhou, C., & Higo, Y. (2015). Sound velocities of $Fe_3Al_2Si_3O_{12}$ almandine up to 19 GPa and 1700 K. *Physics of the Earth and Planetary Interiors*, *246*, 1–8. https://doi.org/10.1016/j.pepi.2015.06.004

Armentrout, M., & Kavner, A. (2011). High pressure, high temperature equation of state for Fe_2SiO_4 ringwoodite and implications for the Earth's transition zone. *Geophysical Research Letters*, *38*, L08309. https://doi.org/10.1029/2011gl046949

Bass, J. D., & Weidner, D. J. (1984). Elasticity of single-crystal orthoferrosilite. *Journal of Geophysical Research*, *89*(B6), 4359–4371. https://doi.org/10.1029/JB089iB06p04359

Belyanin, G. A., Rajesh, H. M., Sajeev, K., & Van Reenen, D. D. (2012). Ultrahigh-temperature metamorphism from an unusual corundum+orthopyroxene intergrowth bearing Al–Mg granulite from the Southern Marginal Zone, Limpopo Complex, South Africa. *Contributions to Mineralogy and Petrology*, *164*(3), 457–475. https://doi.org/10.1007/s00410-012-0747-3

Birch, F. (1947). Finite elastic strain of cubic crystals. *Physical Review*, *71*(11), 809–824. https://doi.org/10.1103/PhysRev.71.809

Bodinier, J. L., & Godard, M. (2007). Orogenic, ophiolitic, and abyssal peridotites. In H. D. Holland & K. K. Turekian (Eds.), *Treatise on Geochemistry* (Vol. 2, pp. 1–73). Pergamon. https://doi.org/10.1016/b0-08-043751-6/02004-1

Chai, M., Brown, J. M., & Slutsky, L. J. (1997). The elastic constants of an aluminous orthopyroxene to 12.5 GPa. *Journal of Geophysical Research*, *102*(B7), 14779–14785. https://doi.org/10.1029/97JB00893

Connolly, J. A. D. (2005). Computation of phase equilibria by linear programming: A tool for geodynamic modeling and its application to subduction zone decarbonation. *Earth and Planetary Science Letters*, *236*(1), 524–541. https://doi.org/10.1016/j.epsl.2005.04.033

de Vries, J., Jacobs, M., vanden Berg, A., Wehber, M., Lathe, C., McCammon, C., & van Westrenen, W. (2013). Thermal equation of state of synthetic orthoferrosilite at lunar pressures and temperatures. *Physics and Chemistry of Minerals*, *40*(9), 691–703. https://doi.org/10.1007/s00269-013-0605-5

Dera, P., Finkelstein, G. J., Duffy, T. S., Downs, R. T., Meng, Y., Prakapenka, V., & Tkachev, S. (2013). Metastable high-pressure transformations of orthoferrosilite Fs_{82}. *Physics of the Earth and Planetary Interiors*, *221*, 15–21. https://doi.org/10.1016/j.pepi.2013.06.006

Dera, P., Zhuravlev, K., Prakapenka, V., Rivers, M. L., Finkelstein, G. J., Grubor-Urosevic, O., et al. (2013). High pressure single-crystal micro X-ray diffraction analysis with GSE_ADA/RSV software. *High Pressure Research*, *33*(3), 466–484. https://doi.org/10.1080/08957959.2013.806504

Dietrich, P., & Arndt, J. (1982). Effects of pressure and temperature on the physical behavior of mantle-relevantolivine, orthopyroxene and garnet: I. Compressibility,thermal propertiesandmacroscopic grüneisen parameters. In W. Schreyer (Ed.), *High-pressure researches in geoscience* (pp. 293–306). Schweizerbart'sche Verlagsbuchhandlung

Dolomanov, O. V., Bourhis, L. J., Gildea, R. J., Howard, J. A., & Puschmann, H. (2009). OLEX2: A complete structure solution, refinement and analysis program. *Journal of Applied Crystallography*, *42*(2), 339–341. https://doi.org/10.1107/S0021889808042726

Dove, M. T. (1997). Theory of displacive phase transitions in minerals. *American Mineralogist*, *82*(3–4), 213–244. https://doi.org/10.2138/am-1997-3-401

Downs, R. T., Zha, C.-S., Duffy, T. S., & Finger, L. W. (1996). The equation of state of forsterite to 17.2 GPa and effects of pressure media. *American Mineralogist*, *81*(1–2), 51–55. https://doi.org/10.2138/am-1996-1-207

Faccenda, M., & Dal Zilio, L. (2017). The role of solid-solid phase transitions in mantle convection. *Lithos*, *268*, 198–224. https://doi.org/10.1016/j.lithos.2016.11.007

Faccincani, L., Faccini, B., Casetta, F., Mazzucchelli, M., Nestola, F., & Coltorti, M. (2021). EoS of mantle minerals coupled with composition and thermal state of the lithosphere: Inferring the density structure of peridotitic systems. *Lithos*, *404–405*, 106483. https://doi.org/10.1016/j.lithos.2021.106483

Fan, D., Fu, S., Yang, J., Tkachev, S. N., Prakapenka, V. B., & Lin, J.-F. (2019). Elasticity of single-crystal periclase at high pressure and temperature: The effect of iron on the elasticity and seismic parameters of ferropericlase in the lower mantle. *American Mineralogist: Journal of Earth and Planetary Materials*, *104*(2), 262–275. https://doi.org/10.2138/am-2019-6656

Fei, Y., Saxena, S. K., & Navrotsky, A. (1990). Internally consistent thermodynamic data and equilibrium phase relations for compounds in the system MgO-SiO_2 at high pressure and high temperature. *Journal of Geophysical Research: Solid*, *95*(B5), 6915–6928. https://doi.org/10.1029/JB095iB05p06915

Finkelstein, G. J., Dera, P. K., & Duffy, T. S. (2015). Phase transitions in orthopyroxene (En_{90}) to 49 GPa from single-crystal X-ray diffraction. *Physics of the Earth and Planetary Interiors*, *244*, 78–86. https://doi.org/10.1016/j.pepi.2014.10.009

Flesch, L. M., Li, B., & Liebermann, R. C. (1998). Sound velocities of polycrystalline $MgSiO_3$-orthopyroxene to 10 GPa at room temperature. *American Mineralogist*, *83*(5), 444–450. https://doi.org/10.2138/am-1998-5-604

Frisillo, A. L., & Barsch, G. R. (1972). Measurement of single-crystal elastic constants of bronzite as a function of pressure and temperature. *Journal of Geophysical Research*, *77*(32), 6360–6384. https://doi.org/10.1029/JB077i032p06360

Frisillo, A. L., & Buljan, S. T. (1972). Linear thermal expansion coefficients of orthopyroxene to 1000°C. *Journal of Geophysical Research*, *77*(35), 7115–7117. https://doi.org/10.1029/JB077i035p07115

Frost, D. J. (2008). The upper mantle and transition zone. *Elements*, *4*(3), 171–176. https://doi.org/10.2113/GSELEMENTS.4.3.171

Fukao, Y., & Obayashi, M. (2013). Subducted slabs stagnant above, penetrating through, and trapped below the 660 km discontinuity. *Journal of Geophysical Research: Solid Earth*, *118*, 5920–5938. https://doi.org/10.1002/2013jb010466

Ganguly, J., Freed, A. M., & Saxena, S. K. (2009). Density profiles of oceanic slabs and surrounding mantle: Integrated thermodynamic and thermal modeling, and implications for the fate of slabs at the 660 km discontinuity. *Physics of the Earth and Planetary Interiors*, *172*(3), 257–267. https://doi.org/10.1016/j.pepi.2008.10.005

Gao, J., Zhu, F., Lai, X.-J., Huang, R., Qin, S., Chen, D.-l., et al. (2014). Compressibility of a natural smithsonite $ZnCO_3$ up to 50 GPa. *High Pressure Research*, *34*(1), 89–99. https://doi.org/10.1080/08957959.2013.868454

Gréaux, S., Kono, Y., Nishiyama, N., Kunimoto, T., Wada, K., & Irifune, T. (2011). *P-V-T* equation of state of $Ca_3Al_2Si_3O_{12}$ grossular garnet. *Physics and Chemistry of Minerals*, *38*(2), 85–94. https://doi.org/10.1007/s00269-010-0384-1

Green, D. H. (1979). Petrogenesis of mid ocean ridge basalts. In M. W. Mcelhinny (Ed.), *The Earth: Its origin, structure and evolution: London* (pp. 200–299). Academic Press.

Hazen, R. M., Papineau, D., Bleeker, W., Downs, R. T., Ferry, J. M., McCoy, T. J., et al. (2008). Mineral evolution. *American Mineralogist*, *93*(11–12), 1693–1720. https://doi.org/10.2138/am.2008.2955

Horiuchi, H., Ito, E., & Weidner, D. J. (1987). Perovskite-type $MgSiO_3$; single-crystal X-ray diffraction study. *American Mineralogist*, *72*(3–4), 357–360

Hua, F. T.-S., Dera, P., & Kung, J. (2020). Compressional behavior of hydrous orthoenstatite: Insight into the nature of LVZ under continental plate. *Minerals*, *10*(1), 71. https://doi.org/10.3390/min10010071

Hugh-Jones, D. (1997). Thermal expansion of $MgSiO_3$ and $FeSiO_3$ ortho-and clinopyroxenes. *American Mineralogist*, *82*(7–8), 689–696. https://doi.org/10.2138/am-1997-7-806

Hugh-Jones, D. A., & Angel, R. J. (1994). A compressional study of $MgSiO_3$ orthoenstatite up to 8.5 GPa. *American Mineralogist*, *79*(5–6), 405–410

Hugh-Jones, D. A., & Angel, R. J. (1997). Effect of Ca^{2+} and Fe^{2+} on the equation of state of $MgSiO_3$ orthopyroxene. *Journal of Geophysical Research*, *102*(B6), 12333–12340. https://doi.org/10.1029/96JB03485

Hugh-Jones, D., Chopelas, A., & Angel, R. (1997). Tetrahedral compression in (Mg, Fe)SiO_3 orthopyroxenes. *Physics and Chemistry of Minerals*, *24*(4), 301–310. https://doi.org/10.1007/s002690050042

Hugh-Jones, D., Sharp, T., Angel, R., & Woodland, A. (1996). The transition of orthoferrosilite to high-pressure *C*2/*c* clinoferrosilite at ambient temperature. *European Journal of Mineralogy*, *8*(6), 1337–1346. https://doi.org/10.1127/ejm/8/6/1337

Ishii, T., & Ohtani, E. (2021). Dry metastable olivine and slab deformation in a wet subducting slab. *Nature Geoscience*, *14*(7), 526–530. https://doi.org/10.1038/s41561-021-00756-7

Ita, J., & Stixrude, L. (1992). Petrology, elasticity, and composition of the mantle transition zone. *Journal of Geophysical Research*, *97*(B5), 6849–6866. https://doi.org/10.1029/92JB00068

Ito, E., & Navrotsky, A. (1985). $MgSiO_3$ ilmenite; calorimetry, phase equilibria, and decomposition at atmospheric pressure. *American Mineralogist*, *70*(9–10), 1020–1026.

Jackson, J. M., Palko, J. W., Andrault, D., Sinogeikin, S. V., Lakshtanov, D. L., Jingyun, W., et al. (2003). Thermal expansion of natural orthoenstatite to 1473 K. *European Journal of Mineralogy*, *15*(3), 469–473. https://doi.org/10.1127/0935-1221/2003/0015-0469

Jackson, J. M., Sinogeikin, S. V., & Bass, J. D. (1999). Elasticity of $MgSiO_3$ orthoenstatite. *American Mineralogist*, *84*, 677–680. https://doi.org/10.2138/am-1999-0421

Jackson, J. M., Sinogeikin, S. V., & Bass, J. D. (2007). Sound velocities and single-crystal elasticity of orthoenstatite to 1073 K at ambient pressure. *Physics of the Earth and Planetary Interiors*, *161*(1–2), 1–12. https://doi.org/10.1016/j.pepi.2006.11.002

Jephcoat, A., Hriljac, J., McCammon, C., O'Neill, H. S. C., Rubie, D., & Finger, L. (1999). High-resolution synchrotron X-ray powder diffraction and Rietveld structure refinement of two ($Mg_{0.95}$, $Fe_{0.05}$)SiO_3 perovskite samples synthesized under different oxygen fugacity conditions. *American Mineralogist*, *84*(3), 214–220. https://doi.org/10.2138/am-1999-0301

Katsura, T., Shatskiy, A., Manthilake, M. G. M., Zhai, S., Yamazaki, D., Matsuzaki, T., et al. (2009). *P-V-T* relations of wadsleyite determined by in situ X-ray diffraction in a large-volume high-pressure apparatus. *Geophysical Research Letters*, *36*, L11307. https://doi.org/10.1029/2009gl038107

King, S. D., Frost, D. J., & Rubie, D. C. (2015). Why cold slabs stagnate in the transition zone. *Geology*, *43*(3), 231–234. https://doi.org/10.1130/G36320.1

Kirby, S. H., Stein, S., Okal, E. A., & Rubie, D. C. (1996). Metastable mantle phase transformations and deep earthquakes in subducting oceanic lithosphere. *Reviews of Geophysics*, *34*(2), 261–306. https://doi.org/10.1029/96RG01050

Klöck, W., Thomas, K., McKay, D., & Palme, H. (1989). Unusual olivine and pyroxene composition in interplanetary dust and unequilibrated ordinary chondrites. *Nature*, *339*(6220), 126–128. https://doi.org/10.1038/339126a0

Kumazawa, M. (1969). The elastic constants of single-crystal orthopyroxene. *Journal of Geophysical Research*, *74*(25), 5973–5980. https://doi.org/10.1029/JB074i025p05973

Kung, J., & Li, B. (2014). Lattice dynamic behavior of orthoferrosilite ($FeSiO_3$) toward phase transition under compression. *Journal of Physical Chemistry C*, *118*(23), 12410–12419. https://doi.org/10.1021/jp4112926

Kung, J., Li, B., Uchida, T., Wang, Y., Neuville, D., & Liebermann, R. C. (2004). In situ measurements of sound velocities and densities across the orthopyroxene-high-pressure clinopyroxene transition in $MgSiO_3$ at high pressure. *Physics of the Earth and Planetary Interiors*, *147*(1), 27–44. https://doi.org/10.1016/j.pepi.2004.05.008

Li, B., Kung, J., Liu, W., & Liebermann, R. C. (2014). Phase transition and elasticity of enstatite under pressure from experiments and first-principles studies. *Physics of the Earth and Planetary Interiors*, *228*, 63–74. https://doi.org/10.1016/j.pepi.2013.11.009

Lin, C.-M., Chao, J., & Lin, C.-C. (2005). Metastable phase transition of orthoenstatite ($MgSiO_3$) under high pressure. *Solid State Sciences*, *7*(3), 293–297. https://doi.org/10.1016/j.solidstatesciences.2004.10.005

Liu, H., Gurnis, M., Leng, W., Jia, Z., & Zhan, Z. (2021). Tonga slab morphology and stress variations controlled by a relic slab: Implications for deep earthquakes in the Tonga-Fiji region. *Geophysical Research Letters*, *48*(7). https://doi.org/10.1029/2020gl091331

Liu, J., Zhang, J., Flesch, L., Li, B., Weidner, D. J., & Liebermann, R. C. (1999). Thermal equation of state of stishovite. *Physics of the Earth and Planetary Interiors*, *112*(3), 257–266. https://doi.org/10.1016/S0031-9201(99)00037-0

Liu, W., & Li, B. (2006). Thermal equation of state of $(Mg_{0.9}Fe_{0.1})_2SiO_4$ olivine. *Physics of the Earth and Planetary Interiors*, *157*(3), 188–195. https://doi.org/10.1016/j.pepi.2006.04.003

Mao, Z., Lin, J.-F., Liu, J., & Prakapenka, V. B. (2011). Thermal equation of state of lower-mantle ferropericlase across the spin crossover. *Geophysical Research Letters*, *38*(23), L23308. https://doi.org/10.1029/2011GL049915

Nesse, W. D. (2000). *Introduction to mineralogy*. Oxford University Press.

Nestola, F. (2015). The crucial role of crystallography in diamond research. *Rendiconti Lincei*, *26*(2), 225–233. https://doi.org/10.1007/s12210-015-0398-1

Nestola, F., Ballaran, T. B., Balic-Zunic, T., Secco, L., & Dal Negro, A. (2008). The high-pressure behavior of an Al- and Fe-rich natural orthopyroxene. *American Mineralogist*, *93*(4), 644–652. https://doi.org/10.2138/am.2008.2693

Nishi, M., Kubo, T., Ohfuji, H., Kato, T., Nishihara, Y., & Irifune, T. (2013). Slow Si-Al interdiffusion in garnet and stagnation of subducting slabs. *Earth and Planetary Science Letters*, *361*, 44–49. https://doi.org/10.1016/j.epsl.2012.11.022

Nishihara, Y., Takahashi, E., Matsukage, K. N., Iguchi, T., Nakayama, K., & Funakoshi, K.-i. (2004). Thermal equation of state of $(Mg_{0.91}Fe_{0.09})_2SiO_4$ ringwoodite. *Physics of the Earth and Planetary Interiors*, *143*, 33–46. https://doi.org/10.1016/j.pepi.2003.02.001

Ono, S., Kikegawa, T., & Higo, Y. (2018). Decomposition boundary from high-pressure clinoenstatite to wadsleyite + stishovite in $MgSiO_3$. *American Mineralogist*, *103*(9), 1512–1515. https://doi.org/10.2138/am-2018-6313CCBY

Periotto, B., Balić-Žunić, T., Nestola, F., Katerinopoulou, A., & Angel, R. J. (2012). Re-investigation of the crystal structure of enstatite under high-pressure conditions. *American Mineralogist*, *97*(10), 1741–1748. https://doi.org/10.2138/am.2012.4157

Reichmann, H. J., Sinogeikin, S. V., Bass, J. D., & Gasparik, T. (2002). Elastic moduli of jadeite-enstatite majorite. *Geophysical Research Letters*, *29*(29), 42–1424. https://doi.org/10.1029/2002gl015106

Ricolleau, A., Fei, Y., Cottrell, E., Watson, H., Deng, L., Zhang, L., et al. (2009). Density profile of pyrolite under the lower mantle conditions. *Geophysical Research Letters*, *36*, L06302. https://doi.org/10.1029/2008GL036759

Ringwood, A. E. (1982). Phase transformations and differentiation in subducted lithosphere: Implications for mantle dynamics, basalt petrogenesis, and crustal evolution. *The Journal of Geology*, *90*, 611–643. https://doi.org/10.1086/628721

Rivers, M., Prakapenka, V. B., Kubo, A., Pullins, C., Holl, C. M., & Jacobsen, S. D. (2008). The COMPRES/GSECARS gas-loading system for diamond anvil cells at the Advanced Photon Source. *High Pressure Research*, *28*(3), 273–292. https://doi.org/10.1080/08957950802333593

Sanehira, T., Irifune, T., Shinmei, T., Ohfuji, H., Brunet, F., & Funakoshi, K.-I. (2008). Density profiles of pyrolite and MORB compositions across the 660 km seismic discontinuity. *High Pressure Research*, *28*(3), 335–349. https://doi.org/10.1080/08957950802251357

Sarver, J., & Hummel, F. (1962). Stability relations of magnesium metasilicate polymorphs. *Journal of the American Ceramic Society*, *45*(4), 152–156. https://doi.org/10.1111/j.1151-2916.1962.tb11110.x

Saxena, S. K. (1988). Assessment of thermal expansion, bulk modulus, and heat capacity of enstatite and forsterite. *Journal of Physics and Chemistry of Solids*, *49*(10), 1233–1235. https://doi.org/10.1016/0022-3697(88)90181-3

Scandolo, L., Mazzucchelli, M. L., Alvaro, M., Nestola, F., Pandolfo, F., & Domeneghetti, M. C. (2015). Thermal expansion behaviour of orthopyroxenes: The role of the Fe-Mn substitution. *Mineralogical Magazine*, *79*(1), 71–87. https://doi.org/10.1180/minmag.2015.079.1.07

Serghiou, G., Boehler, R., & Chopelas, A. (2000). Reversible coordination changes in crystalline silicates at high pressure and ambient temperature. *Journal of Physics: Condensed Matter*, *12*(6), 849–857. https://doi.org/10.1088/0953-8984/12/6/309

Shekar, N. C., & Rajan, K. G. (2001). Kinetics of pressure induced structural phase transitions—A review. *Bulletin of Materials Science*, *24*(1), 1–21. https://doi.org/10.1007/bf02704834

Sheldrick, G. M. (2008). A short history of SHELX. *Acta Crystallographica Section A*, *64*(Pt 1), 112–122. https://doi.org/10.1107/S0108767307043930

Shinmei, T., Tomioka, N., Fujino, K., Kuroda, K., & Irifune, T. (1999). In situ X-ray diffraction study of enstatite up to 12 GPa and 1473 K and equations of state. *American Mineralogist*, *84*, 1588–1594. https://doi.org/10.2138/am-1999-1012

Sinogeikin, S. V., & Bass, J. D. (2000). Single-crystal elasticity of pyrope and MgO to 20 GPa by Brillouin scattering in the diamond cell. *Physics of the Earth and Planetary Interiors*, *120*(1), 43–62. https://doi.org/10.1016/S0031-9201(00)00143-6

Sinogeikin, S. V., & Bass, J. D. (2002). Elasticity of majorite and a majorite-pyrope solid solution to high pressure: Implications for the transition zone. *Geophysical Research Letters*, *29*(2), 4–144. https://doi.org/10.1029/2001GL013937

Smith, E. M., Shirey, S. B., Richardson, S. H., Nestola, F., Bullock, E. S., Wang, J., & Wang, W. (2018). Blue boron-bearing diamonds from Earth's lower mantle. *Nature*, *560*(7716), 84–87. https://doi.org/10.1038/s41586-018-0334-5

Stachel, T., & Harris, J. W. (2008). The origin of cratonic diamonds — constraints from mineral inclusions. *Ore Geology Reviews*, *34*(1), 5–32. https://doi.org/10.1016/j.oregeorev.2007.05.002

Sueno, S., Cameron, M., & Prewitt, C. (1976). Orthoferrosilite: High-temperature crystal chemistry. *American Mineralogist*, *61*(1–2), 38–53.

Tamura, A., & Arai, S. (2006). Harzburgite–dunite–orthopyroxenite suite as a record of supra-subduction zone setting for the Oman ophiolite mantle. *Lithos*, *90*(1), 43–56. https://doi.org/10.1016/j.lithos.2005.12.012

Tarantino, S. C., Domeneghetti, M. C., Carpenter, M. A., Shaw, C. J., & Tazzoli, V. (2002). Mixing properties of the enstatite-ferrosilite solid solution: I. A macroscopic perspective. *European Journal of Mineralogy*, *14*(3), 525–536. https://doi.org/10.1127/0935-1221/2002/0014-0525

Tribaudino, M., & Mantovani, L. (2014). Thermal expansion in *C2/c* pyroxenes: A review and new high-temperature structural data for a pyroxene of composition $(Na_{0.53}Ca_{0.47})(Al_{0.53}Fe_{0.47})Si_2O_6$ ($Jd_{53}Hd_{47}$). *Mineralogical Magazine*, *78*(2), 311–324. https://doi.org/10.1180/minmag.2014.078.2.06

Van Mierlo, W., Langenhorst, F., Frost, D., & Rubie, D. (2013). Stagnation of subducting slabs in the transition zone due to slow diffusion in majoritic garnet. *Nature Geoscience*, *6*(5), 400–403. https://doi.org/10.1038/ngeo1772

Walter, M., Kohn, S., Araujo, D., Bulanova, G., Smith, C., Gaillou, E., et al. (2011). Deep mantle cycling of oceanic crust: Evidence from diamonds and their mineral inclusions. *Science*, *334*(6052), 54–57. https://doi.org/10.1126/science.1209300

Wang, J., Bass, J. D., & Kastura, T. (2014). Elastic properties of iron-bearing wadsleyite to 17.7GPa: Implications for mantle mineral models. *Physics of the Earth and Planetary Interiors*, *228*, 92–96. https://doi.org/10.1016/j.pepi.2014.01.015

Wang, S., Chen, T., Cai, N., Qi, X., Fiege, A., Liebermann, R. C., & Li, B. (2019). Pressure-induced velocity softening in natural orthopyroxene at mantle temperature. *American Mineralogist: Journal of Earth and Planetary Materials*, *104*(8), 1173–1179. https://doi.org/10.2138/am-2019-6935

Webb, S. L., & Jackson, I. (1993). The pressure dependence of the elastic moduli of single-crystal orthopyroxene $(Mg_{0.8}Fe_{0.2})SiO_3$. *European Journal of Mineralogy*, *5*, 1111–1120. https://doi.org/10.1127/ejm/5/6/1111

Weidner, D. J., Wang, H., & Ito, J. (1978). Elasticity of orthoenstatite. *Physics of the Earth and Planetary Interiors*, *17*(2), P7–P13. https://doi.org/10.1016/0031-9201(78)90043-2

Woodland, A. B. (1998). The orthorhombic to high-P monoclinic phase transition in Mg-Fe Pyroxenes: Can it produce a seismic discontinuity? *Geophysical Research Letters*, *25*(8), 1241–1244. https://doi.org/10.1029/98gl00857

Workman, R. K., & Hart, S. R. (2005). Major and trace element composition of the depleted MORB mantle (DMM). *Earth and Planetary Science Letters*, *231*(1), 53–72. https://doi.org/10.1016/j.epsl.2004.12.005

Xu, J., Fan, D., Zhang, D., Guo, X., Zhou, W., & Dera, P. K. (2020). Phase transition of enstatite-ferrosilite solid solutions at high pressure and high temperature: Constraints on metastable orthopyroxene in cold subduction. *Geophysical Research Letters*, *47*(12), e2020GL087363. https://doi.org/10.1029/2020GL087363

Xu, J., Zhang, D., Dera, P., Zhang, B., & Fan, D. (2017). Experimental evidence for the survival of augite to transition zone depths, and implications for subduction zone dynamics. *American Mineralogist*, *102*(7), 1516–1524. https://doi.org/10.2138/am-2017-5959

Xu, J., Zhang, D., Fan, D., Dera, P. K., Shi, F., & Zhou, W. (2019). Thermoelastic properties of eclogitic garnets and omphacites: Implications for deep subduction of oceanic crust and density anomalies in the upper mantle. *Geophysical Research Letters*, *46*, 179–188. https://doi.org/10.1029/2018GL081170

Xu, J., Zhang, D., Fan, D., Zhang, J. S., Hu, Y., Guo, X., et al. (2018). Phase transitions in orthoenstatite and subduction zone dynamics: Effects of water and transition metal ions. *Journal of Geophysical Research: Solid Earth*, *123*, 2723–2737. https://doi.org/10.1002/2017JB015169

Xu, Z., Ma, M., Li, B., Hong, X., Han, L., & Zhou, X. (2016). The elasticity of natural hypersthene and the effect of Fe and Al substitution. *High Pressure Research*, *36*, 1–72. https://doi.org/10.1080/08957959.2015.1136623

Xu, Z., Ma, M., Li, B., Hong, X., Han, L., & Zhou, X. (2017). Compressibility and thermal expansion of hypersthene. *High Temperatures - High Pressures*, *46*(1)

Yang, H., & Ghose, S. (1994). Thermal expansion, Debye temperature and Grüneisen parameter of synthetic (Fe, Mg)SiO_3 orthopyroxenes. *Physics and Chemistry of Minerals*, *20*(8), 575–586. https://doi.org/10.1007/BF00211853

Zhang, D., Dera, P. K., Eng, P. J., Stubbs, J. E., Zhang, J. S., Prakapenka, V. B., et al. (2017). High pressure single crystal diffraction at PX^2. *Journal of Visualized Experiments: JoVE*, *119*, e54660. Retrieved from https://www.jove.com/video/54660

Zhang, D., Jackson, J. M., Chen, B., Sturhahn, W., Zhao, J., Yan, J., & Caracas, R. (2013). Elasticity and lattice dynamics of enstatite at high pressure. *Journal of Geophysical Research: Solid Earth*, *118*, 4071–4082. https://doi.org/10.1002/jgrb.50303

Zhang, D., Jackson, J. M., Sturhahn, W., & Xiao, Y. (2011). Local structure variations observed in orthoenstatite at high pressures. *American Mineralogist*, *96*(10), 1585–1592. https://doi.org/10.2138/am.2011.3721

Zhang, J. S., & Bass, J. D. (2016). Single crystal elasticity of natural Fe-bearing orthoenstatite across a high-pressure phase transition. *Geophysical Research Letters*, *43*, 8473–8481. https://doi.org/10.1002/2016GL069963

Zhang, J. S., Dera, P., & Bass, J. D. (2012). A new high-pressure phase transition in natural Fe-bearing orthoenstatite. *American Mineralogist*, *97*(7), 1070–1074. https://doi.org/10.2138/am.2012.4072

Zhang, J. S., Reynard, B., Montagnac, G., & Bass, J. D. (2014). Pressure-induced *Pbca–P*$2_1/c$ phase transition of natural orthoenstatite: The effect of high temperature and its geophysical implications. *Physics of the Earth and Planetary Interiors*, *228*, 150–159. https://doi.org/10.1016/j.pepi.2013.09.008

Zhang, J. S., Reynard, B., Montagnac, G., Wang, R. C., & Bass, J. D. (2013). Pressure-induced *Pbca-P*$2_1/c$ phase transition of natural orthoenstatite: Compositional effect and its geophysical implications. *American Mineralogist*, *98*(5–6), 986–992. https://doi.org/10.2138/am.2013.4345

Zhang, L., Ahsbahs, H., Hafner, S. S., & Kutoglu, A. (1997). Single-crystal compression and crystal structure of clinopyroxene up to 10 GPa. *American Mineralogist*, *82*(3), 245–258. https://doi.org/10.2138/am-1997-3-402

Zhao, Y., Dreele, R. V., Zhang, J., & Weidner, D. (1998). Thermoelastic equation of state of monoclinic pyroxene: $CaMgSi_2O_6$ diopside. *The Review of High Pressure Science and Technology*, *7*, 25–27. https://doi.org/10.4131/jshpreview.7.25

Zhao, Y., Schiferl, D., & Shankland, T. J. (1995). A high PT single-crystal X-ray diffraction study of thermoelasticity of $MgSiO_3$ orthoenstatite. *Physics and Chemistry of Minerals*, *22*(6), 393–398. https://doi.org/10.1007/BF00213337

Zhao, Y., Von Dreele, R. B., Shankland, T. J., Weidner, D. J., Zhang, J., Wang, Y., & Gasparik, T. (1997). Thermoelastic equation of state of jadeite $NaAlSi_2O_6$: An energy-dispersive Reitveld Refinement Study of low symmetry and multiple phases diffraction. *Geophysical Research Letters*, *24*(1), 5–8. https://doi.org/10.1029/96GL03769

Zou, Y., Gréaux, S., Irifune, T., Whitaker, M. L., Shinmei, T., & Higo, Y. (2012). Thermal equation of state of $Mg_3Al_2Si_3O_{12}$ pyrope garnet up to 19 GPa and 1,700 K. *Physics and Chemistry of Minerals*, *39*(7), 589–598. https://doi.org/10.1007/s00269-012-0514-z